AIAA JOURNAL
Vol. 46, No. 11, November 2008

Formulation of the k-ω Turbulence Model Revisited

David C. Wilcox*
DCW Industries, Inc., La Cañada, California 91011

DOI: 10.2514/1.36541

This paper presents a reformulated version of the author's k-ω model of turbulence. Revisions include the addition of just one new closure coefficient and an adjustment to the dependence of eddy viscosity on turbulence properties. The result is a significantly improved model that applies to both boundary layers and free shear flows and that has very little sensitivity to finite freestream boundary conditions on turbulence properties. The improvements to the k-ω model facilitate a significant expansion of its range of applicability. The new model, like preceding versions, provides accurate solutions for mildly separated flows and simple geometries such as that of a backward-facing step. The model's improvement over earlier versions lies in its accuracy for even more complicated separated flows. This paper demonstrates the enhanced capability for supersonic flow into compression corners and a hypersonic shock-wave/boundary-layer interaction. The excellent agreement is achieved without introducing any compressibility modifications to the turbulence model.

Nomenclature

$C_{\lim}$	=	stress-limiter coefficient
C_p	=	pressure coefficient, $(p - p_\infty)/(\frac{1}{2}\rho U_\infty^2)$
c	=	chord length
c_f	=	skin-friction coefficient
D_k	=	dissipation of turbulence kinetic energy
E	=	Favre-averaged total energy, $\rho(e + \frac{1}{2}u_i u_i + k)$
e	=	Favre-averaged specific internal energy
f_β	=	round-jet function
H	=	backward-facing-step height
h	=	Favre-averaged specific enthalpy
k	=	Favre-averaged specific turbulence kinetic energy
k_s, k_s^+	=	dimensional and dimensionless surface-roughness height, $u_\tau k_s/\nu_w$
M_∞	=	freestream Mach number
p	=	mean static pressure, finite-difference-scheme order of accuracy
p_w, p_∞	=	surface and freestream mean static pressure
P_k	=	production of turbulence kinetic energy
Pr_L, Pr_T	=	laminar and turbulent Prandtl number
Re_H, Re_θ	=	Reynolds number based on step height and momentum thickness
Re_∞	=	Reynolds number per unit length
r	=	fine-grid point to coarse-grid point number ratio
S_R, S_B	=	dimensionless surface value of ω for a surface with roughness and mass injection
S_{ij}	=	Favre-averaged strain-rate tensor, $\frac{1}{2}(\partial u_i/\partial x_j + \partial u_j/\partial x_i)$
$\bar{S}_{ij}$	=	zero-trace Favre-averaged strain-rate tensor, $S_{ij} - \frac{1}{3}\partial u_m/\partial x_m \delta_{ij}$
$\hat{S}_{ij}$	=	Galilean-invariant Favre-averaged strain-rate tensor, $S_{ij} - \frac{1}{2}\partial u_m/\partial x_m \delta_{ij}$
T_w, T_{aw}	=	Favre-averaged wall temperature, adiabatic wall temperature
t	=	time
t_{ij}	=	mean viscous stress tensor
U_e, U_∞	=	Favre-averaged boundary-layer-edge and freestream velocity
u	=	Favre-averaged streamwise x velocity component
u_i	=	Favre-averaged velocity vector
u_τ	=	friction velocity
v_w, v_w^+	=	dimensional and dimensionless vertical surface mass-injection velocity, v_w/u_τ
x	=	streamwise coordinate
x_i	=	position vector
x_r, x_s	=	reattachment and separation point
y	=	surface-normal coordinate
α, β, σ, σ_d	=	closure coefficients in the specific dissipation-rate equation
β^*, σ^*	=	closure coefficients in the turbulence-kinetic-energy equation
δ	=	boundary-layer thickness
δ'	=	free-shear-layer spreading rate, $\mathrm{d}\delta/\mathrm{d}x$
δ'_o	=	value of δ' for $\omega_\infty \to 0$ (k-ω model) or $\varepsilon_\infty \to 0$ (k-ε model)
δ_{ij}	=	Kronecker delta
ε	=	dissipation rate
θ	=	momentum thickness
μ, μ_T	=	molecular, eddy viscosity
ν, ν_w	=	local and surface value of the kinematic molecular viscosity
ρ	=	mean mass density
σ_{do}	=	value of σ_d when $\partial k/\partial x_i \partial\omega/\partial x_i > 0$
τ_{ij}	=	Favre-averaged specific Reynolds-stress tensor
τ_{xy}	=	Favre-averaged specific Reynolds shear stress
χ_p	=	Pope's nondimensional measure of vortex stretching parameter
χ_ω	=	absolute value of χ_p
Ω	=	Mean vorticity
Ω_{ij}	=	rotation tensor, $\frac{1}{2}(\partial u_i/\partial x_j - \partial u_j/\partial x_i)$
ω	=	specific dissipation rate
$\tilde{\omega}$	=	effective specific dissipation rate used to compute eddy viscosity

Presented as Paper 1408 at the 45th AIAA Aerospace Sciences Meeting and Exhibit, Reno, NV, 8–11 January 2007; received 8 January 2008; revision received 29 May 2008; accepted for publication 13 June 2008.

*President, 5354 Palm Drive. Associate Fellow AIAA.

I. Introduction

THE k-ω model was first created independently by Kolmogorov [1] and later by Saffman [2]. Wilcox and Alber [3] and Wilcox [4,5] have continually refined and improved the model during the past three decades and demonstrated its accuracy for a wide range of turbulent flows. This paper presents the author's latest efforts aimed at improving the model.

The new model incorporates two key modifications: namely, the addition of a cross-diffusion term and a built-in stress-limiter

modification that makes the eddy viscosity a function of k, ω, and the ratio of turbulence-energy production to turbulence-energy dissipation.

The addition of cross diffusion to the ω equation was first suggested by Speziale et al. [6] as a remedy for the original k-ω model's sensitivity to the freestream value of ω. Although Speziale et al. (as well as, for example, Menter [7], Wilcox [8], Kok [9], and Hellsten [10]) have succeeded in using cross diffusion to eliminate boundary-condition sensitivity, it has come at the expense of the ability to make reasonable predictions for free shear flows. Strictly speaking, models created in this spirit are limited in applicability to wall-bounded flows.

Coakley [11] introduced the stress-limiter modification. Huang [12] showed, in detail, that by limiting the magnitude of the eddy viscosity when turbulence-energy production exceeds turbulence-energy dissipation, this modification yields larger separation bubbles and, most notably, greatly improves incompressible- and transonic-flow predictions. Kandula and Wilcox [13] verified for a transonic airfoil that it improves predictive accuracy of the baseline k-ω model without cross diffusion and blending functions and/or nonlinear constitutive relations such as those implemented by Menter [7] and Hellsten [10]. In point of fact, the success achieved in this paper demonstrates that blending functions are an unnecessary complication.

Although these ideas are not new, the way they were implemented is new. The k-ω model was reformulated using the methodology developed by Wilcox [14] in which boundary layers and free shear flows are first dissected and analyzed using perturbation methods and similarity solutions. All aspects of the model, including boundary conditions for rough surfaces and surfaces with mass injection, were reformulated and validated. Then a series of computations was performed for nearly 100 different applications, including free shear flows, attached boundary layers, backward-facing steps, and separated flows. The test cases cover all Mach-number ranges from incompressible through hypersonic. Wilcox [14] presented complete details of the model's formulation, including all of the analysis, software, input data, and experimental data used in developing and testing the model. This paper includes results of the new k-ω model's most significant applications.

II. New k-ω Model

For the sake of clarity, this paper will refer to the reformulated k-ω equations as the new k-ω model. This paper focuses on what's new about the model relative to previous versions. Readers interested in all aspects of the model and its development can find a complete presentation by Wilcox [14].

A. Mean-Flow Equations

The Favre-averaged equations for conservation of mass, momentum, and energy are as follows:

$$\frac{\partial \rho}{\partial t} + \frac{\partial}{\partial x_i}(\rho u_i) = 0 \tag{1}$$

$$\frac{\partial}{\partial t}(\rho u_i) + \frac{\partial}{\partial x_j}(\rho u_j u_i) = -\frac{\partial p}{\partial x_i} + \frac{\partial}{\partial x_j}(t_{ji} + \rho\tau_{ji}) \tag{2}$$

$$\frac{\partial}{\partial t}\left[\rho\left(e + \frac{1}{2}u_i u_i + k\right)\right] + \frac{\partial}{\partial x_j}\left[\rho u_j\left(h + \frac{1}{2}u_i u_i + k\right)\right] = \frac{\partial}{\partial x_j}\left[u_i(t_{ij} + \rho\tau_{ij}) + \left(\frac{\mu}{\mathrm{Pr}_L} + \frac{\mu_T}{\mathrm{Pr}_T}\right)\frac{\partial h}{\partial x_j} + \left(\mu + \sigma^*\frac{\rho k}{\omega}\right)\frac{\partial k}{\partial x_j}\right] \tag{3}$$

Note that the energy-conservation equation (3) ensures conservation of total energy E, which includes the kinetic energy of the turbulence. Consequently, the equation's diffusion term includes the explicit appearance of the molecular and turbulent diffusion of k.

B. Constitutive Equations

The model uses the following equations to compute the molecular and specific Reynolds-stress tensors:

$$t_{ij} = 2\mu\bar{S}_{ij}, \qquad \rho\tau_{ij} = 2\mu_T\bar{S}_{ij} - \frac{2}{3}\rho k\delta_{ij} \tag{4}$$

$$\bar{S}_{ij} = S_{ij} - \frac{1}{3}\frac{\partial u_k}{\partial x_k}\delta_{ij} \tag{5}$$

$$\mu_T = \frac{\rho k}{\tilde{\omega}}, \qquad \tilde{\omega} = \max\left\{\omega, C_{\lim}\sqrt{\frac{2\bar{S}_{ij}\bar{S}_{ij}}{\beta^*}}\right\} \tag{6}$$

$$C_{\lim} = \tfrac{7}{8} \tag{7}$$

The stress-limiter modification [Eq. (6)] uses the zero-trace version of the mean strain-rate tensor (viz., $\bar{S}_{ij}$). Some turbulence-model researchers prefer the magnitude of the vorticity vector in place of $(2\bar{S}_{ij}\bar{S}_{ij})^{1/2}$. Using the magnitude of the vorticity with $C_{\lim} = 0.95$ is satisfactory for shock-separated-flow predictions up to Mach 3 (and possibly a bit higher). However, numerical experimentation with this k-ω model has shown that it has a detrimental effect on hypersonic shock-induced separation, some (but not all) attached boundary layers, and some free shear flows (especially the mixing layer).

C. Turbulence Model Equations

The equations governing the turbulence kinetic energy and specific dissipation rate are

$$\frac{\partial}{\partial t}(\rho k) + \frac{\partial}{\partial x_j}(\rho u_j k) = \rho\tau_{ij}\frac{\partial u_i}{\partial x_j} - \beta^*\rho k\omega + \frac{\partial}{\partial x_j}\left[\left(\mu + \sigma^*\frac{\rho k}{\omega}\right)\frac{\partial k}{\partial x_j}\right] \tag{8}$$

$$\frac{\partial}{\partial t}(\rho\omega) + \frac{\partial}{\partial x_j}(\rho u_j\omega) = \alpha\frac{\omega}{k}\rho\tau_{ij}\frac{\partial u_i}{\partial x_j} - \beta\rho\omega^2 + \sigma_d\frac{\rho}{\omega}\frac{\partial k}{\partial x_j}\frac{\partial\omega}{\partial x_j} + \frac{\partial}{\partial x_j}\left[\left(\mu + \sigma\frac{\rho k}{\omega}\right)\frac{\partial\omega}{\partial x_j}\right] \tag{9}$$

The turbulence-kinetic-energy equation (8) contains no special compressibility terms involving pressure work, diffusion, or dilatation. Although a dilatation–dissipation modification to the k equation improves compressible mixing-layer predictions (see Wilcox [14]), the same modification has a detrimental effect on shock-separated-flow predictions. Hence, it is omitted from the k equation for general applications.

Note that the turbulent-diffusion terms in Eqs. (8) and (9) (i.e., the terms proportional to σ^* and σ) are proportional to $\rho k/\omega$ rather than to the eddy viscosity. This means that the only terms in these equations that are implicitly affected by the stress limiter are the production terms (via the Reynolds-stress tensor). Consequently, the new k-ω model can serve as the foundation of a model with a more general prescription for computing the Reynolds-stress tensor such as an algebraic stress model, a full stress-transport model, and even a detached eddy simulation. In principle, there should be no need to revise the model's closure coefficients to accommodate an alternative way of computing the Reynolds stresses. Wilcox [14] demonstrated this flexibility for a stress-transport model.

D. Closure Coefficients

The various closure coefficients appearing in the new k-ω model are

$$\alpha = \tfrac{13}{25}, \qquad \beta^* = \tfrac{9}{100}, \qquad \sigma = \tfrac{1}{2}, \qquad \sigma^* = \tfrac{3}{5}, \qquad Pr_T = \tfrac{8}{9} \tag{10}$$

$$\sigma_d = \begin{cases} 0, & \frac{\partial k}{\partial x_j}\frac{\partial \omega}{\partial x_j} \le 0 \\ \sigma_{do}, & \frac{\partial k}{\partial x_j}\frac{\partial \omega}{\partial x_j} > 0 \end{cases}, \qquad \sigma_{do} = \frac{1}{8} \tag{11}$$

$$\beta = \beta_o f_\beta, \qquad \beta_o = 0.0708, \qquad f_\beta = \frac{1 + 85\chi_\omega}{1 + 100\chi_\omega} \tag{12}$$

$$\chi_\omega \equiv \left| \frac{\Omega_{ij}\Omega_{jk}\hat{S}_{ki}}{(\beta^*\omega)^3} \right|, \qquad \hat{S}_{ki} = S_{ki} - \frac{1}{2}\frac{\partial u_m}{\partial x_m}\delta_{ki} \tag{13}$$

The round-jet parameter χ_ω is computed with $\hat{S}_{ki}$, which, unlike the compressible strain rate recommended by Papp and Dash [15], is Galilean-invariant. This is necessary because using S_{ki} or $\bar{S}_{ki}$ yields undesired effects in two-dimensional compressible flows.

E. Boundary Condition for Rough and Smooth Surfaces

For surfaces that include surface roughness, the model uses the no-slip condition for velocity and k. The surface value of ω depends upon the dimensionless surface-roughness height k_s^+. The boundary condition for ω is

$$\omega = \frac{u_\tau^2}{\nu} S_R \quad \text{at } y = 0 \tag{14}$$

where S_R was chosen to provide a close match to measured rough-surface boundary-layer data of Nikuradse, as noted in [16]. The following correlation between S_R and k_s^+ reproduces measured effects of sand-grain roughness for values of k_s^+ up to about 400:

$$S_R = \begin{cases} (\frac{200}{k_s^+})^2, & k_s^+ \le 5 \\ \frac{100}{k_s^+} + [(\frac{200}{k_s^+})^2 - \frac{100}{k_s^+}]e^{5-k_s^+}, & k_s^+ > 5 \end{cases} \tag{15}$$

A surface is considered to be hydraulically smooth when $k_s^+ < 5$. For such surfaces, we can combine Eqs. (14) and (15) to obtain the slightly-rough-surface boundary condition for ω: namely,

$$\omega = \frac{40,000\nu}{k_s^2} \quad \text{at } y = 0 \tag{16}$$

Because the turbulence-model solution for a hydraulically smooth surface is nearly identical to the perfectly smooth-surface solution, Eq. (16) can be used for smooth surfaces, with k_s chosen to insure that $k_s^+ < 5$.

F. Boundary Condition for a Surface with Mass Transfer

For a surface with mass transfer, we again implement the no-slip condition for the mean velocity and k. When the surface has blowing corresponding to $v_w > 0$, the boundary condition for ω is

$$\omega = \frac{u_\tau^2}{\nu} S_B \quad \text{at } y = 0 \tag{17}$$

where the value of S_B was chosen to achieve optimum agreement between measured [17] and computed velocities. The correlation between S_B and dimensionless mass-injection velocity v_w^+ is given in analytical form as

$$S_B = \frac{25}{v_w^+(1 + 5v_w^+)} \tag{18}$$

When the surface has suction corresponding to $v_w < 0$, the value of ω appropriate for a smooth surface [Eq. (16)] should be used.

III. Cross Diffusion

One of the key modifications in the new k-ω model is addition of a cross-diffusion term. The term proportional to σ_d in Eq. (9) is referred to as cross diffusion. It depends upon gradients of both k and ω.

A. Free Shear Flows

In free shear flows the cross-diffusion term enhances production of ω, which in turn increases dissipation of k (assuming $\sigma_d > 0$). This occurs for small freestream values of k and ω, for which both quantities decrease approaching the shear-layer edge. The overall effect is to reduce the net production of k, which reduces the predicted spreading rates.

Several authors, including Speziale et al., [6] Menter [7], Wilcox [8], Peng et al. [18], Kok [9], and Hellsten [10], have attempted to improve the k-ω model by adding cross diffusion. Although all have achieved some degree of success in wall-bounded flows, the models are far less realistic for free shear flows. Inspection of Table 1 shows that spreading rates predicted by such models differ significantly from measured values.

Menter [7] and Hellsten [10] enjoyed more success with cross diffusion than Speziale et al. [6] and Peng et al. [18]. Both introduced blending functions that cause all of the model's closure coefficients to assume values appropriate for the k-ω model near solid boundaries and to asymptotically approach values similar to those used with the k-ε model [19] otherwise. The net result is a model that behaves very much like the Wilcox [4] k-ω model for wall-bounded flows and more like the k-ε model for free shear flows.

Wilcox [8] and, more recently, Kok [9] tried a similar concept with the cross-diffusion coefficient σ_d, given by

$$\sigma_d = \begin{cases} 0, & \frac{\partial k}{\partial x_j}\frac{\partial \omega}{\partial x_j} \le 0 \\ \sigma_{do}, & \frac{\partial k}{\partial x_j}\frac{\partial \omega}{\partial x_j} > 0 \end{cases} \tag{19}$$

Additionally, σ^* assumes a value larger than $\frac{1}{2}$. It is important to suppress the cross-diffusion term close to solid boundaries for wall-bounded flows. This is true because, as discussed in detail by Wilcox [14], cross diffusion changes the near-surface structure of the ω equation in a way that undermines sublayer predictions. Just as Menter's blending function causes σ_d to approach zero near a solid boundary, so does Eq. (19), because k increases and ω decreases in the viscous sublayer. Although simpler than Menter's blending-function approach, Wilcox [8] and Kok [9] chose values for σ_{do} that yield free-shear-layer spreading rates that are farther from measurements than those predicted by the k-ε model. Specifically, Wilcox [8] set $\sigma_{do} = \frac{3}{10}$, $\sigma = \frac{3}{5}$, and $\sigma^* = 1$, whereas Kok [9] opted for $\sigma_{do} = \sigma = \frac{1}{2}$ and $\sigma^* = \frac{2}{3}$.

However, other values of the k-ω model's closure coefficients exist that yield closer agreement with measured spreading rates. Note

Table 1 Two-equation model free-shear-flow spreading rates

Flow	Speziale [6]	Peng [18]	Kok [9]	Wilcox [4]	New k-ω	Measured
Far wake	0.221	0.206	0.191	0.496	0.326	0.320–0.400
Mixing layer	0.082	0.071	0.056	0.141	0.096	0.103–0.120
Plane jet	0.089	——	0.083	0.135	0.108	0.100–0.110
Round jet	0.102	0.096	0.107	0.369	0.094	0.086–0.096
Radial jet	0.073	0.040	0.068	0.317	0.099	0.096–0.110

first that, based on the analysis of a turbulent front by Lele [20], there are two necessary conditions for the front to propagate. Specifically, we must have

$$\sigma_{do} > \sigma^* - \sigma \quad \text{and} \quad \sigma^* > \sigma_{do} \tag{20}$$

Figure 1 shows how predicted spreading rates vary with σ_{do} for the far wake, the mixing layer, and the plane jet. The curves shown were computed with all other closure coefficients as specified in Eqs. (10) and (12). To isolate effects of cross diffusion, results shown correspond to having no stress limiter: that is, $\tilde{\omega} = \omega$ in Eq. (6). The limiter has virtually no effect on the far wake and the plane jet. It reduces the mixing-layer spreading rate by less than 6%. Of greatest relevance to the present discussion, the value of σ^* is $3/5$. As shown, spreading rates for all three cases are greatest when σ_{do} is equal to its minimum permissible value according to Eq. (20) (viz., $\sigma_{do} = \sigma^* - \sigma$). Predicted values decrease monotonically as σ_{do} increases and fall below the lower bound of measured spreading rates for all three cases when $\sigma_{do} = \frac{1}{5}$, which is much less than the maximum allowable value of $\frac{3}{5}$.

Figure 2 shows how predicted spreading rates vary with σ^* when we set σ_{do} equal to its minimum permissible value. As noted, computations were done with all closure coefficients other than σ^*, as specified in Eqs. (10) and (12) in the absence of the stress limiter. Computed spreading rates for all three cases decrease monotonically as σ^* increases. Computed δ' values lie above the range of measured δ' for all three cases when $\sigma^* < 0.55$ and below when $\sigma^* < 0.70$. Thus, we conclude that

$$0.55 < \sigma^* < 0.70 \qquad (\text{for } \sigma = \tfrac{1}{2}) \tag{21}$$

These results provide the rationale for selecting $\sigma^* = \frac{3}{5}$ and $\sigma_{do} = \frac{1}{8}$ for the new k-ω model.

B. Round-Jet/Plane-Jet Anomaly

Inspection of Table 1 shows that, with the exception of the new k-ω model, all of the turbulence models listed predict that the round jet spreads more rapidly than the plane jet. Measurements indicate the opposite trend, with the round-jet spreading rate being about 10% lower than that of the plane jet. This shortcoming, common to most turbulence models, is known as the *round-jet/plane-jet anomaly*.

Pope [21] proposed a modification to the ε equation that resolves the round-jet/plane-jet anomaly for the k-ε model [19]. In Pope's modification, the *dissipation of dissipation* term in the ε equation is replaced by

$$C_{\varepsilon 2}\frac{\varepsilon^2}{k} \to [C_{\varepsilon 2} - C_{\varepsilon 3}\chi_p]\frac{\varepsilon^2}{k} \tag{22}$$

where $C_{\varepsilon 2}$ and $C_{\varepsilon 3}$ are closure coefficients. In terms of k-ω model parameters, $\varepsilon \propto k\omega$. The parameter χ_p is a nondimensional measure of vortex stretching defined as

$$\chi_p \equiv \frac{\Omega_{ij}\Omega_{jk}S_{ki}}{(\varepsilon/k)^3} \tag{23}$$

Pope's [21] reasoning is that the primary mechanism for transfer of energy from large to small eddies is vortex stretching. Any mechanism that enhances vortex stretching will increase this rate of transfer. Because the energy is being transferred to the smallest eddies in which dissipation occurs, the dissipation must necessarily increase. Because mean-flow vortex lines cannot be stretched in a two-dimensional flow, χ_p is zero for the plane jet. By contrast, the vortex-stretching parameter is nonzero for an axisymmetric mean flow. As argued by Pope, this corresponds to the fact that vortex rings are stretched radially. Thus, we expect to have $\chi_p \neq 0$ for a round jet.

Using $C_{\varepsilon 3} = 0.79$ reduces the k-ε model's predicted spreading rate to 0.86, consistent with measurements. However, as pointed out by Rubel [22], the Pope [21] correction has an adverse effect on

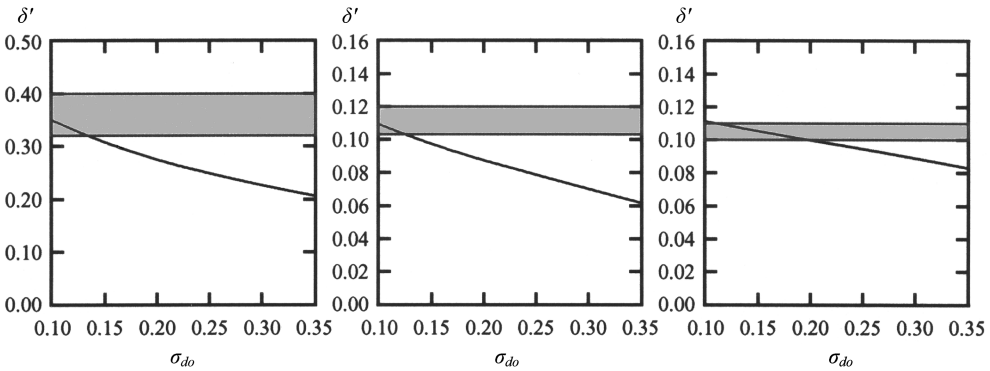

a) Far wake b) Mixing layer c) Plane jet

Fig. 1 Effect of cross diffusion on free-shear-flow spreading rates for $\sigma^* = \frac{3}{5}$ and $\sigma = \frac{1}{2}$; shaded areas depict measured-value ranges.

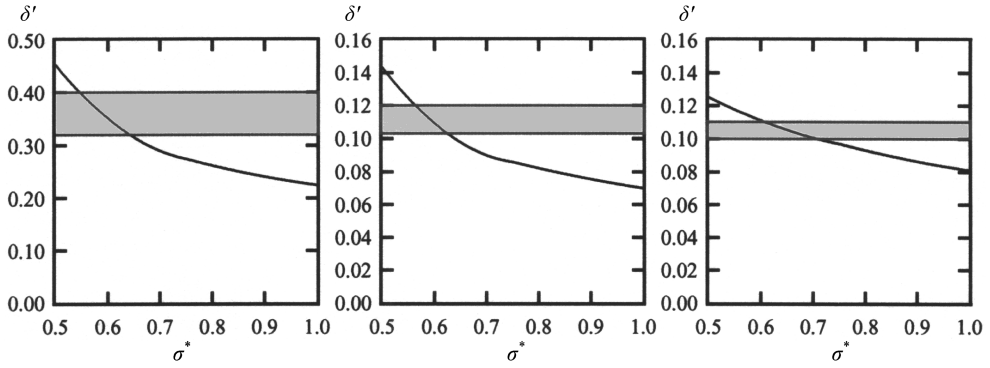

a) Far wake b) Mixing layer c) Plane jet

Fig. 2 Effect of cross diffusion on free-shear-flow spreading rates for $\sigma_{do} = \sigma^* - \sigma$ and $\sigma = \frac{1}{2}$; shaded areas depict measured-value ranges.

model predictions for the radial jet, which also has nonzero χ_p. Without the Pope correction, the k-ε model predicts a radial-jet spreading rate of 0.094, which is close to the measured range of 0.096 to 0.110 (see Tanaka and Tanaka [23] and Witze and Dwyer [24]). Using the Pope [21] correction for the radial jet reduces the k-ε model-predicted spreading rate to 0.040. Hence, as noted by Rubel [22], "the round jet/plane jet anomaly has been exchanged for a round jet/radial jet anomaly."

In contrast to the k-ε model, as indicated in Table 1, the Wilcox [4] k-ω model predicts comparable spreading rates for both the round and radial jets, both larger than the predicted plane-jet spreading rate. Similarly, when a constant value of $\beta = 0.0708$ is used for the new k-ω model, the predicted round- and radial-jet spreading rates are 0.177 and 0.168, respectively. Numerical experimentation shows that if β is reduced to 0.06, the model's spreading rates for both the round and radial jets are close to the measured values. Because Pope's [21] argument implies nothing regarding the functional dependence of the modification upon χ_p, it is completely consistent to propose that β depends upon this parameter in a manner that reduces the value of β as needed for both flows. Thus, as a generalization of the Pope modification, the reformulated k-ω model uses the following prescription for β:

$$\beta = \beta_o f_\beta \tag{24}$$

where

$$\beta_o = 0.0708, \qquad f_\beta = \frac{1 + 85\chi_\omega}{1 + 100\chi_\omega} \tag{25}$$

and

$$\chi_\omega \equiv \left| \frac{\Omega_{ij}\Omega_{jk}S_{ki}}{(\beta^*\omega)^3} \right| \tag{26}$$

Comparison of Eqs. (23) and (26) shows that $\chi_\omega = |\chi_p|$. Also, the functional form of f_β is such that its asymptotic value is 0.85, so that $\beta = 0.06$ for large values of χ_ω. Finally, note that the vortex-stretching parameter normally is very small in axisymmetric boundary layers because ω is very large.

Although the usefulness of Pope's [21] correction as represented by Eqs. (22) and (23) is limited by a flaw in the k-ε model, the concepts underlying the formulation are not. We can reasonably conclude that Pope's analysis provides a sensible reflection of the physics of turbulent jets, at least in the context of ω-based two-equation models.

C. Computed and Measured Velocity Profiles

Figure 3 illustrates the remarkable effect that a modest amount of cross diffusion has upon free-shear-flow results. For reference, the figure includes results obtained for the standard k-ε model [19] and for the renormalization group (RNG) k-ε model [25]. Experimental data for the far wake are from Fage and Falkner [26] and Weygandt and Mehta [27], whereas those for the radially spreading jet are from Witze and Dwyer [24].

D. Sensitivity to Finite Freestream Boundary Conditions

Two-equation models have a unique and unexpected feature when nonzero freestream boundary conditions are specified for k, ω, ε, etc. Specifically, even if we select k and the second turbulence property (ω, ε, etc.) to be sufficiently small that both k and ν_T are negligible, the solution is sensitive to our choice of the second turbulence property's freestream value. This is an important consideration because most computations are done with these assumptions.

Figure 4 shows how the spreading rate δ'/δ'_o varies with the freestream value of ω for the new k-ω model and the Wilcox [4] k-ω model for the far wake, the mixing layer, and the plane jet. It also shows the variation of δ' with the freestream value of ε for the standard k-ε model [19]. All computations were done with the same (very small) dimensionless eddy viscosity.

All three models predict a decrease in spreading rate as the freestream value of ω or ε increases. In all three graphs, the freestream value is scaled with respect to the value at $y = 0$, which is either equal to or very close to the maximum value for each flow. As shown, without cross diffusion, the k-ω model displays a strong sensitivity to the freestream value of ω. The addition of cross diffusion greatly reduces the sensitivity. The k-ε model predicts very little sensitivity to the freestream value of ε. The graphs also show that if the freestream value is less than 1% of the maximum value [$\omega_\infty/\omega(x,0) < 0.01$, $\varepsilon_\infty/\varepsilon(x,0) < 0.01$], there is virtually no effect on the predicted spreading rate. This is certainly not an unreasonable constraint, because using a freestream value of ω or ε in excess of 1% of the peak value would very likely correspond to using a physically unrealistic value.

There is no mystery about why the solution should have some sensitivity to freestream boundary conditions. We are, after all, solving a two-point boundary-value problem, which requires

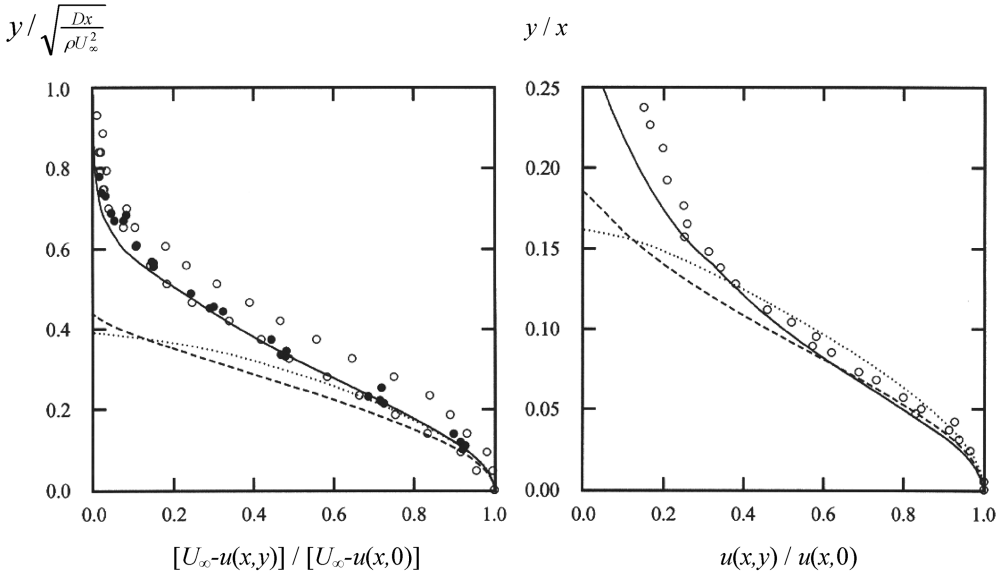

Fig. 3 Far-wake and radially spreading-jet solutions: new k-ω model (solid line), k-ε model [19] (dashed line), RNG k-ε model [25] (dotted line), and measured [24,26,27] (open and filled circles).

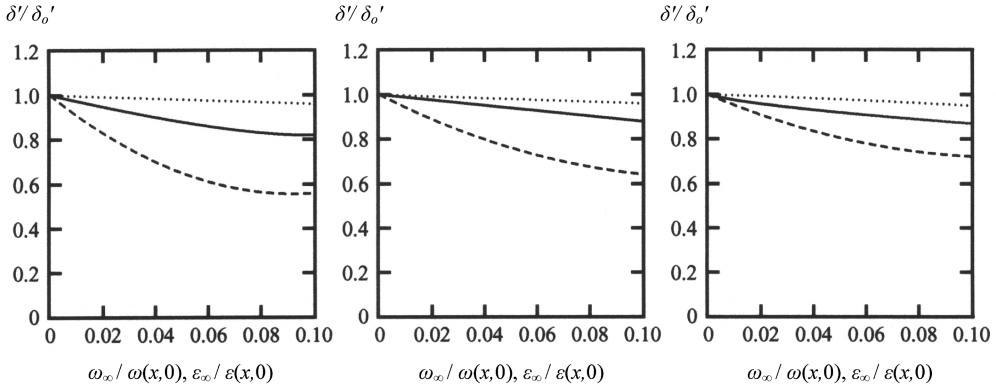

Fig. 4 Sensitivity of free-shear-flow spreading rates to freestream conditions: new k-ω model (solid line), Wilcox [4] k-ω model (dashed line), and k-ε model [19] (dotted line).

freestream boundary conditions on all variables, including ω and ε. In light of this, it is clear that there must be some range of boundary values that affect the solution. Figure 4 shows that there is a well-defined limiting form of the solution for vanishing freestream boundary values.

It is the odd nature of the differential equation for ε that makes the k-ε model much less sensitive to freestream conditions than the k-ω model. Specifically, because its dissipation term is proportional to ε^2/k, the equation is singular as $k \to 0$ for finite freestream values of ε. This unusual behavior of the ε equation obviates the need to invest enough thought to avoid prescribing physically unrealistic freestream values for a quantity such as ε. Although this may be comforting to engineers who do not care to invest such thought, turbulent-fluid-flow applications exist [14] for which being sloppy with freestream boundary conditions can foil the protection provided by the ε equation.

Studies have been published [28] in which the freestream value of ω has been set to very large values. With an extremely large freestream ω, any k-ω model solution for many flows, especially free shear flows, will be grossly distorted. This type of analysis is very misleading because having freestream values of ω more than a percent or so of the maximum value in the turbulent region is physically incorrect. What ω quantifies is the vorticity of the energy-containing eddies. Assigning huge values of ω in the freestream would imply that there is significant fluctuating vorticity above the turbulent region, which is absurd.

As an analogy, consider the laminar boundary layer with zero pressure gradient. The boundary-layer equations admit a similarity solution (viz., the Blasius solution). Imagine that rather than imposing the freestream boundary condition on the velocity, we specify the freestream value of the vorticity. For zero freestream vorticity, the solution is identical to the Blasius solution. Figure 5 shows how the skin friction varies with the freestream vorticity Ω_∞. There is significant distortion when Ω_∞ exceeds a 100th of a percent (0.01%) of the peak vorticity Ω_o in the boundary layer. How different is this from selecting a physically unrealistic freestream boundary condition on the vorticity of the energy-containing eddies with the k-ω model? *The same logic that would cite the sensitivity to a freestream value of ω that exceeds 1% of the peak value in the turbulent region as a flaw in the turbulence model would conclude that Prandtl's boundary-layer equations are fundamentally flawed for the same reason!*

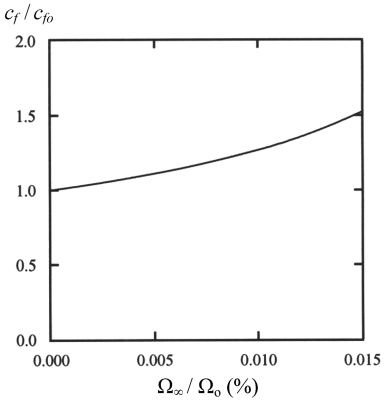

Fig. 5 Effect of freestream vorticity on an incompressible laminar flat-plate boundary layer.

E. Attached Boundary Layers

As demonstrated by Kok [9], cross diffusion does not necessarily cause a loss of accuracy in predicting effects of pressure gradient on attached boundary layers. This is true of the new k-ω model. Figure 6 compares computed and measured skin-friction and velocity profiles for two attached boundary layers with a strong adverse pressure gradient. The graphs to the left correspond to the classic Samuel–Joubert experiment [29], which has an increasingly adverse gradient. This is an important test case that was poorly predicted by virtually all turbulence models at the 1980–81 AFOSR-HTTM-Stanford Conference on Complex Turbulent Flows [29]. The graphs to the right correspond to the incipient-separation case of Stratford [30]. To this author's knowledge, this prediction is the closest to measurements of any turbulence model used to predict the flow. Virtually all k-ε models, for example, predict skin friction that is 4 times the measured value.

The new k-ω model, as with previous versions, applies equally well to supersonic and even hypersonic boundary layers. Figure 7 compares computed and measured velocity profiles for Mach 4.5 and Mach 10.3 flat-plate boundary layers [31]. Note that $U^+ = u^*/u_\tau$, where u^* is the van Driest (see Wilcox [14]) scaled velocity.

F. Turbulent/Nonturbulent Interfaces

More often than not, turbulence-model equations that are in general usage appear to predict sharp interfaces between turbulent and nonturbulent regions (i.e., interfaces in which discontinuities in derivatives of flow properties occur at the edge of the shear layer). As noted by Wilcox [14], these interfaces bear no relation to the physical turbulent/nonturbulent interfaces that actually fluctuate in time and have smooth Reynolds-averaged properties. Omitting details of the analysis for the sake of brevity, for the k-ω model with cross diffusion included (but no stress limiter), the asymptotic behavior of u, k, and ω approaching a turbulent/nonturbulent interface is given by

$$\left.\begin{array}{c} U_e - u \sim u_o(1 - y/\delta)^{n_u} \\ k \sim k_o(1 - y/\delta)^{n_k} \\ \omega \sim \omega_o(1 - y/\delta)^{n_\omega} \end{array}\right\} \quad \text{as} \quad y \to \delta \tag{27}$$

where u_o, k_o, and ω_o are integration constants and the three exponents are

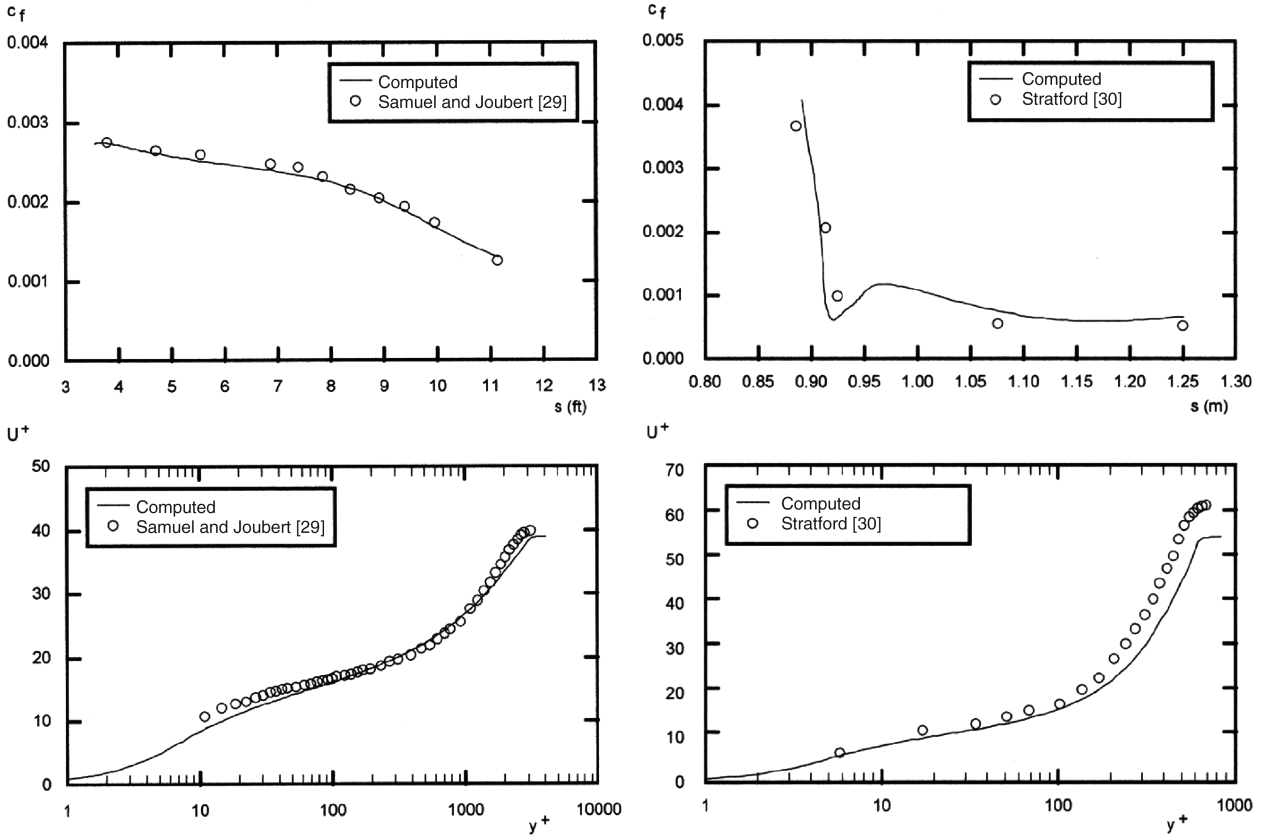

Fig. 6 Attached boundary layers with strong adverse pressure gradient: computed values (solid line) and Samuel and Joubert experiment [29] (circles) and Stratford [30] (circles).

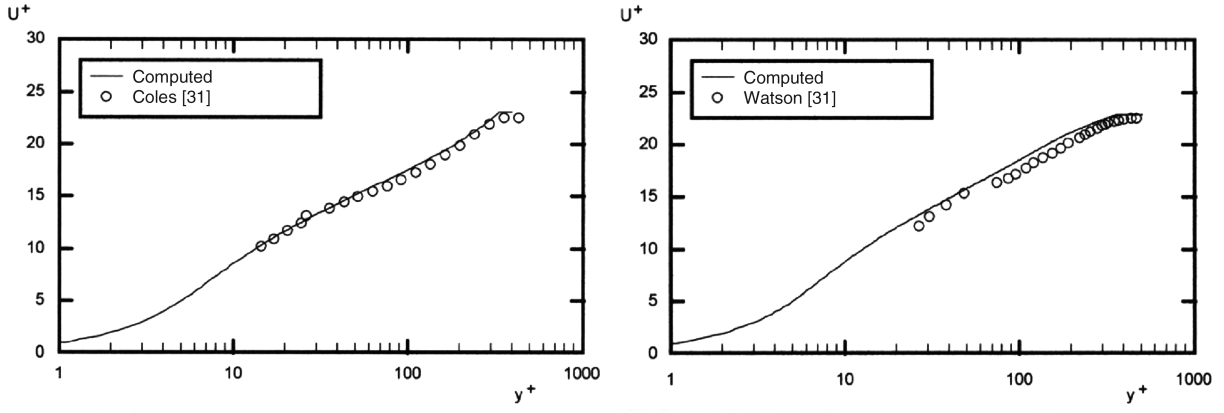

a) Mach 4.5 **b) Mach 10.3**

Fig. 7 Supersonic and hypersonic boundary layers: Coles experiment [31] (circles) and Watson experiment [31] (circles).

$$\left.\begin{aligned} n_u &= \frac{\sigma\sigma^*}{\sigma-\sigma^*+\sigma_{do}} \\ n_k &= \frac{\sigma}{\sigma-\sigma^*+\sigma_{do}} \\ n_\omega &= \frac{\sigma^*-\sigma_{do}}{\sigma-\sigma^*+\sigma_{do}} \end{aligned}\right\} \tag{28}$$

With a stress limiter included, n_k and n_ω are unchanged, but the solution for the velocity is such that $n_u = n_k$.

For the solution to give $u \to U_e$, $k \to 0$, and $\omega \to 0$ as we approach the turbulent/nonturbulent interface from the turbulent side, all three exponents in Eqs. (28) must be positive. This is true provided the closure coefficients σ, σ^*, and σ_{do} satisfy the following constraints:

$$\sigma_{do} > \sigma^* - \sigma \quad \text{and} \quad \sigma^* > \sigma_{do} \tag{29}$$

These are identical to the constraints deduced by Lele [20] in analyzing a turbulent front. Table 2 lists the values of the exponents for several k-ω models, each having unique behavior.

1) Hellsten's [10] model features continuous second derivatives for u, k, and ω, so that its weak-solution behavior should be of no consequence in a second-order-accurate numerical solution.

Table 2 Turbulent/nonturbulent interface exponents for k-ω models

Model	σ	σ^*	σ_{do}	n_u	n_k	n_ω
Hellsten [10]	1.000	1.100	0.400	3.333	3.333	2.333
Kok [9]	0.500	0.667	0.500	1.000	1.500	0.500
Menter [7]	0.856	1.000	1.712	0.546	0.546	−0.454
New k-ω	0.500	0.600	0.125	20	20	19

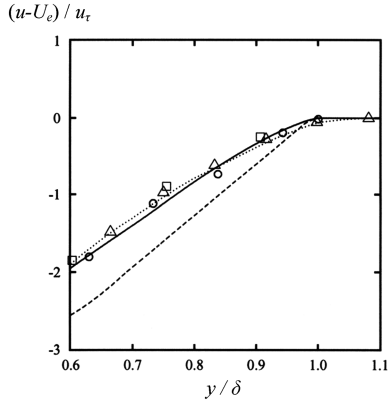

Fig. 8 Computed and measured velocity defect near the boundary-layer edge for a flat-plate boundary layer using three k-ω models: new (solid line), Kok (dashed line), Hellsten (dotted line), Klebanoff (circles), Wieghardt and Tillman [33] (squares), and Winter and Gaudet [34] (triangles).

2) Kok's [9] model has classic weak-solution behavior with discontinuities in the slope of u and ω.

3) Because Menter's [7] model fails to satisfy the second condition of Eq. (29), the solution for ω approaches ∞ as $y \to \delta$.

4) The new k-ω model is analytic approaching the interface so that it does not have a nonphysical weak-solution behavior.

Hellsten [10] made the case for choosing the values of the model's closure coefficients based on achieving smooth solution behavior at a turbulent/nonturbulent interface. Part of Hellsten's arguments include a claim that to achieve such behavior it is necessary to have $\sigma^* > 1$. Because the new k-ω model has a completely analytical solution at such an interface while having $\sigma^* < 1$, a closer look is in order.

Figure 8 compares computed and measured [32–34] velocity profiles in the immediate vicinity of the boundary-layer edge for a constant-pressure boundary layer. Hellsten [10] presented a similar graph showing the linear approach of Kok's [9] velocity profile and the discontinuity in slope at the interface. By contrast, both the Hellsten [10] model and the new k-ω model exhibit a smooth approach to freestream values, with both curves falling within experimental-data scatter.

The apparent contradiction in Hellsten's [10] claim regarding the minimum value of σ^* needed to achieve smooth solutions near a turbulent/nonturbulent interface is easily resolved. Inspection of Fig. 8 shows that below $y/\delta \approx 0.95$ all three velocity profiles are very nearly linear functions of y/δ. The region in which the asymptotic solution given in Eqs. (27) and (28) is valid lies well within the upper 1–5% of the boundary layer, depending on the precise values of n_u, n_k, and n_ω. Consequently, on the scale shown in the graph, it is difficult to discern much difference between the solutions for the Hellsten model and the new k-ω model. As noted, both models have continuous second derivatives (and higher) approaching the interface and should be expected to cause no troublesome numerical issues to arise.

IV. Stress Limiter

The second key modification in the new k-ω model occurs in the expression for the eddy viscosity. In the new model, ν_T is the ratio of k to ω multiplied by a factor that is, effectively, a function of the turbulence-kinetic-energy production-to-dissipation ratio. This modification greatly improves the model's predictions for supersonic and hypersonic separated flows.

Note that this modification pertains to the proposed constitutive relation between the Reynolds stresses and mean-flow properties, rather than to the k-ω model per se. The virtues of the stress limiter (often referred to as a weakly nonlinear stress/strain-rate relationship) can be realized by using a nonlinear stress/strain-rate relationship or even by computing the Reynolds stresses with a stress-transport model based on the k and ω equations. As noted earlier, because the stress limiter appears in the k and ω equations only through the Reynolds-stress tensor, the new k-ω model can be used, without modification, with other prescriptions for the Reynolds stresses. Wilcox [14], for example, presented complete details for a k-ω-based stress-transport model.

Coakley [11] was the first to suggest that shock-separated flows can be more accurately simulated with the k-ω model by simply limiting the magnitude of the Reynolds shear stress when production of turbulence kinetic energy exceeds its dissipation. He developed a stress limiter that showed some promise for improving k-ω model predictions. Menter [7], Kandula and Wilcox [13], Durbin [35], and Huang [12], for example, subsequently confirmed the effectiveness of a stress limiter for flow speeds up to the transonic range.

Durbin [35] and Moore and Moore [36] assessed the realizability of turbulence-energy production predicted using the Boussinesq approximation. They observed that for flows such as impinging jets and the inviscid highly strained flow approaching a stagnation point, without the assistance of a stress limiter, the Boussinesq approximation leads to unrealistically high turbulence-energy levels: levels that are not realized in nature. Moore and Moore proposed the following general relation for limiting the Reynolds stress. Letting $\mu_T = \rho k/\tilde{\omega}$, they proposed that $\tilde{\omega}$ is given by

$$\tilde{\omega} = \max\left\{\omega, \quad C_0\omega + C_{\lim}\sqrt{\frac{2\lambda_1\bar{S}_{ij}\bar{S}_{ij} + 2\lambda_2\Omega_{ij}\Omega_{ij}}{(\lambda_1+\lambda_2)\beta^*}}\right\} \tag{30}$$

Table 3 lists the values of the constants C_0, $C_{\lim}$, λ_1, and λ_2 proposed by several researchers.

To understand the way in which the stress limiter suppresses the magnitude of the Reynolds shear stress, we first simplify Eq. (30) for the most commonly used version that has $C_0 = 0$, $\lambda_1 = 1$, and $\lambda_2 = 0$: namely,

$$\tilde{\omega} = \max\left\{\omega, \quad C_{\lim}\sqrt{\frac{2\bar{S}_{ij}\bar{S}_{ij}}{\beta^*}}\right\} \tag{31}$$

In a shear layer, we know that $2\bar{S}_{ij}\bar{S}_{ij} \approx (\partial u/\partial y)^2$. So Eq. (31) tells us that

$$\rho\tau_{xy} = \mu_T\frac{\partial u}{\partial y} = \min\left\{\frac{\rho k}{\omega}\frac{\partial u}{\partial y}, \quad C_{l_{\lim}}^{-1}\sqrt{\beta^*}\rho k\right\} \tag{32}$$

Also, observe that in the absence of a stress limiter, the ratio of production to dissipation in the equation for turbulence kinetic energy is

$$\frac{P_k}{D_k} = \frac{(\rho k/\omega)(\partial u/\partial y)^2}{\beta^*\rho k\omega} = \left(\frac{\partial u/\partial y}{\sqrt{\beta^*\omega}}\right)^2 \tag{33}$$

Thus, the stress-limiter modification is such that

$$\rho\tau_{xy} = C_{l_{\lim}}^{-1}\sqrt{\beta^*}\rho k \quad \text{for} \quad \frac{P_k}{D_k} \geq C_{l_{\lim}}^{-2} \tag{34}$$

Consequently, the stress limiter drives the Reynolds shear stress toward the form Bradshaw et al. [37] implemented in their one-equation turbulence model. When $C_{\lim} = 1$, the coefficient $C_{\lim}^{-1}(\beta^*)^{1/2} = 0.30$, which matches the value of Bradshaw's

Table 3 Stress-limiter coefficients

Reference	C_0	$C_{\lim}$	λ_1	λ_2
Coakley [11]	0	1.00	1	0
Durbin [35]	0	1.03	1	0
Menter [7]	0	1.00	0	1
Moore and Moore [36]	2.85	0.75	1	1
New k-ω	0	0.88	1	0

constant [14]. For the new k-ω model, we find that $C_{\lim}^{-1}(\beta^*)^{1/2} = 0.34$.

Interestingly, in a shear layer the turbulence-kinetic-energy production term in the Saffman and Wilcox [38] k-ω^2 model is $P_k = 0.30\rho k|\partial u/\partial y|$. Hence, production of k is constrained although the eddy viscosity is not. This is the reason that Wilcox and Traci [39] were able to accurately compute the increase in turbulence kinetic energy approaching a stagnation point. This is not possible with a two-equation turbulence model that does not implement a stress limiter (Durbin [35]), because the strain-rate field is such that P_k/D_k is typically in excess of 100. Although experimental data are not shown in Fig. 9, the computed amplification is consistent with the measurements of Bearman [40].

Figure 10 shows the dramatic improvement in predicted pressure coefficient for Mach 0.8 flow past a NACA 0012 airfoil at a 2.26 deg angle of attack [13]. The solid curves identified as original correspond to the Wilcox [4] k-ω model, which does not use a stress limiter. The dashed curves identified as SST correspond to the same model with a stress limiter applied using $C_{\lim} = 1$. The most dramatic difference is the location of the shock. Without the stress limiter, the predicted shock location is farther downstream than the measured location. Adding the stress limiter increases the size of the separation bubble on the upper surface of the airfoil, causing the computed shock location to lie much closer to the experimentally observed location.

The following subsections compare computed and measured flow properties for separated flows with flow speeds from incompressible to hypersonic. All computations were done using a second-order-accurate Navier–Stokes solver developed by MacCormack [41]. In every case, generalized Richardson extrapolation was performed and Appendix A summarizes the results.

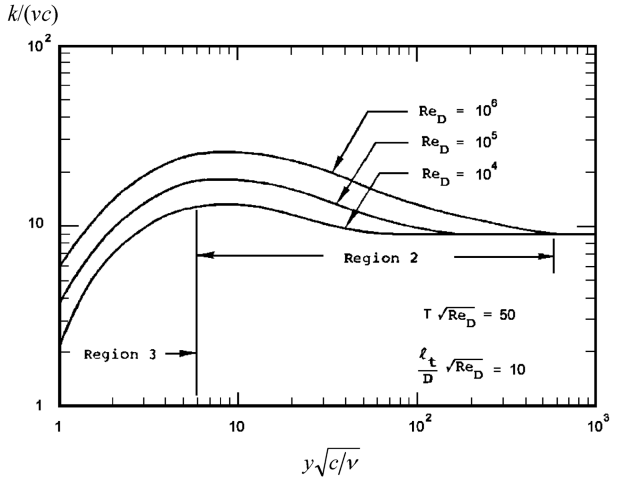

Fig. 9 Variation of turbulence kinetic energy approaching a stagnation point; Saffman-Wilcox [38] k-ω^2 model (solid lines).

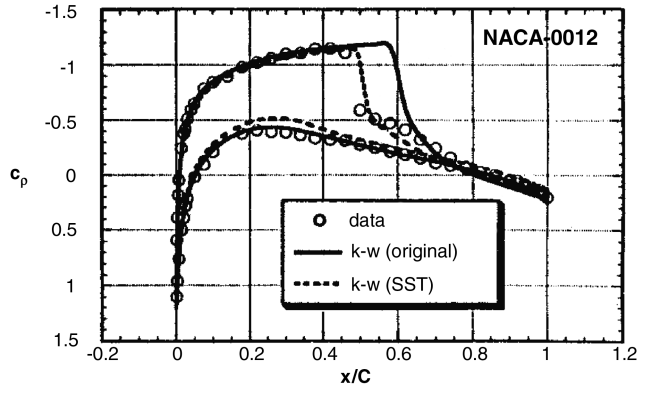

Fig. 10 Comparison of computed and measured surface pressure for transonic flow past a NACA 0012 airfoil at a 2.26 deg angle of attack.

A. Incompressible Backward-Facing Steps

We first consider the backward-facing step of Driver and Seegmiller [42]. Figure 11 compares computed and measured skin-friction and surface-pressure coefficients for the new k-ω model. The figure also includes values predicted by the Wilcox [4] k-ω model to help discern the effect of the stress limiter. With the exception of the reattachment point, all computed flow properties are nearly identical. The only significant difference is the reattachment length, which is 13% longer with the stress limiter. Menter [7] found a similar effect in his computations.

Flow past a backward-facing step is mildly dependent on Reynolds number. As summarized by Jovic and Driver [43], reattachment length is somewhat shorter at low Reynolds numbers. To assess the effect of Reynolds number on k-ω model backward-facing-step predictions, we now consider the case documented by Jovic and Driver [44]. Reynolds number based on step height for the Jovic–Driver backward-facing-step experiment is $Re_H = 5000$. By contrast, the considered Driver–Seegmiller case has $Re_H = 37,500$.

Figure 12 compares computed and measured skin-friction and surface-pressure coefficients. Both versions of the k-ω model predict c_f and C_p variations that fall within a few percent of measured values over most of the flowfield. Predicted reattachment length is $6.64H$ (a 7% *increase* over the $Re_H = 37,500$ prediction) for the Wilcox [4] k-ω model and $7.28H$ (a 3% *increase*) for the new k-ω model. Because the measured length is $6.00H$ (a 4% *decrease*), neither model reflects the measured reduction of recirculation-region length.

These two examples show that using the stress limiter with the k-ω model increases the size of the separated region. The stress limiter increases differences between predicted and measured reattachment length for flow past backward-facing steps (Figs. 11 and 12). This is understandable because the model yields reattachment lengths that are very close to measured lengths in the absence of the stress limiter.

To gain some insight into the stress limiter's nature, recall that we compute the eddy viscosity according to Eq. (6). In implementing the stress-limiter concept for his hybrid k-ω/k-ε model, Menter [7] selected $C_{\lim} = 1$ and excluded it from the hybrid ω/ε equation. Durbin [35] recommended $C_{\lim} = 1.03$ for use with a pure k-ω model.

Figure 13 indicates how reattachment length for the $Re_H = 37,500$ backward-facing step varies with $C_{\lim}$. As shown, x_r increases in a monotone fashion as $C_{\lim}$ increases. The asymptotic value in the absence of a stress limiter (i.e., for $C_{\lim} = 0$) is

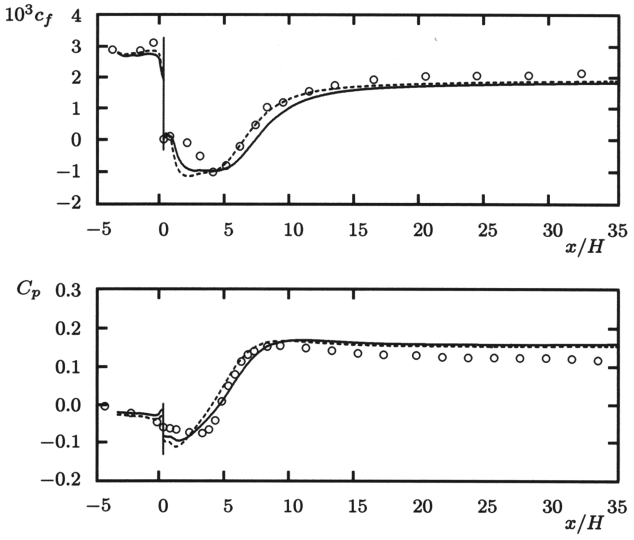

Fig. 11 Computed and measured skin friction and surface pressure for flow past a backward-facing step; $Re_H = 37,500$: new k-ω model (solid line) Wilcox [4] k-ω model (dashed line), and Driver-Seegmiller [42] (circles).

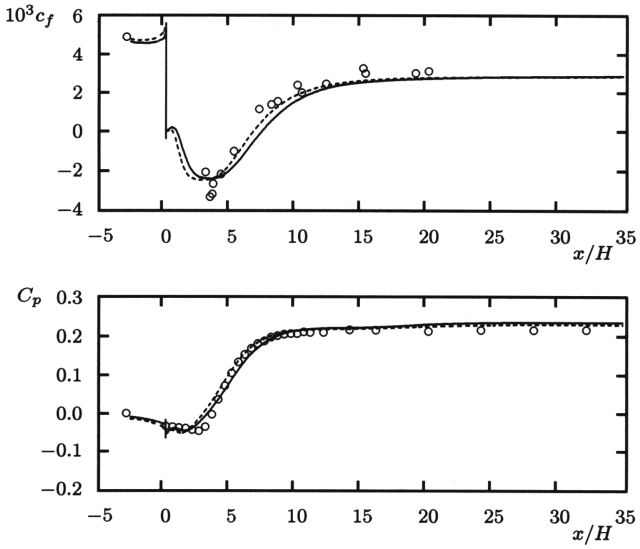

Fig. 12 Computed and measured skin friction and surface pressure for flow past a backward-facing step; $Re_H = 5000$; new k-ω model (solid line), Wilcox [4] k-ω model (dashed line), and Jovic and Driver [44] (circles).

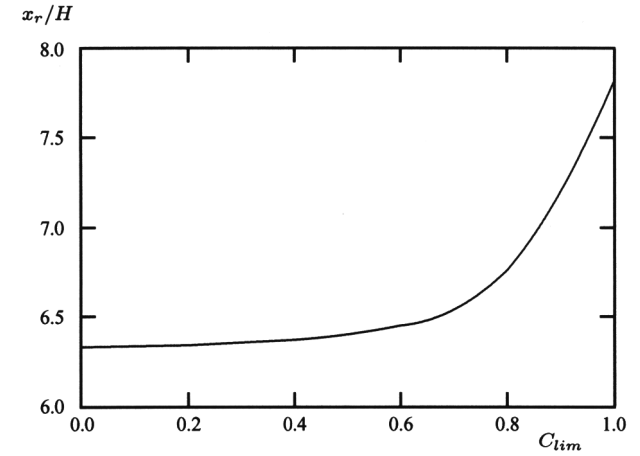

Fig. 13 Effect of the stress-limiter coefficient on computed reattachment length for a backward-facing step with $Re_H = 37,500$.

$x_r = 6.33H$, which is 1% larger than the measured value. Selecting $C_{\text{lim}} = 7/8$ yields a value of $x_r = 7.07H$, which is within 13% of the measured length.

B. Transonic Flow Over an Axisymmetric Bump

The transonic-bump experiment of Bachalo and Johnson [45] is a particularly challenging separated-flow application. In the experiment, a long slender bump is fared onto the surface of a cylinder. The freestream Mach number is $M_\infty = 0.875$, the unit Reynolds number is $Re_\infty = 4 \times 10^6$ ft^{-1}, and the surface is adiabatic. A shock wave develops over the bump, which separates the boundary layer. The flow reattaches in the wake of the bump, giving rise to a reattachment shock. This flow is very difficult to predict because the bump surface pressure is extremely sensitive to the size of the separation bubble, which is strongly coupled to the precise shock locations.

Figure 14 compares computed and measured C_p for four turbulence models. The short-dashed curve corresponds to the Wilcox [4] k-ω model, which does not have a stress limiter. Although the predicted separation-shock location differs from the measured location by only 6% of the bump's chord length, computed and measured C_p differ significantly. The solid curve corresponds to the new k-ω model, which includes a stress limiter. Differences between computed and measured C_p are generally less than 7%. The

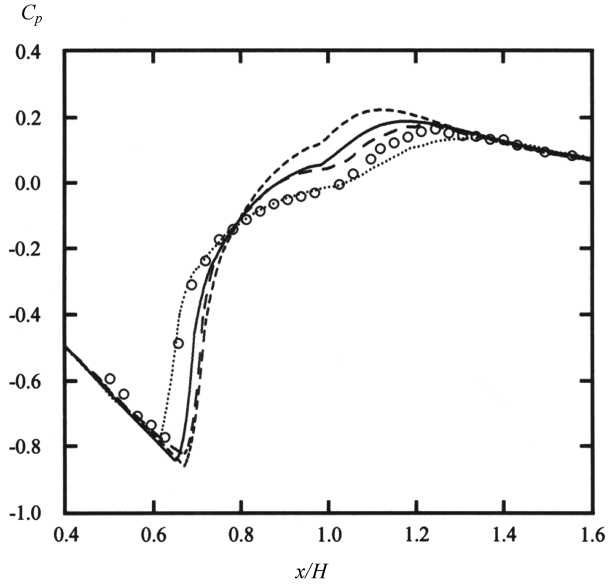

Fig. 14 Application of several turbulence models to transonic flow past an axisymmetric bump: new k-ω (solid line), Wilcox [4] k-ω (dashed line), Menter [7] k-ω/k-ε (dotted line), Spalart–Allmaras [46] (wide dashed line), and Bachalo and Johnson [45] (circles).

long-dashed curve corresponds to the Spalart–Allmaras [46] one-equation model. Although separation-shock location and separation are about the same as for the Wilcox [4] model, computed C_p is closer to measured C_p near reattachment. The dotted curve corresponds to Menter's [7] k-ω/k-ε model with a stress limiter. Computed and measured shock locations and C_p are quite close.

Using $C_{\text{lim}} = 1$ with the new k-ω model yields C_p nearly identical to the Menter [7] prediction. But the improved results for this flow come at the expense of much greater discrepancies between theory and experiment for both smaller and larger Mach numbers. This explains why Menter's model, which appears to be fine-tuned for the transonic regime, fares well for Mach numbers from incompressible up to transonic speeds, but very poorly for supersonic and hypersonic flows. The primary culprit is not so much the stress-limiter strength, as reflected by the value of C_{lim}, as it is the Boussinesq approximation. By accepting 7% discrepancies between predicted and measured properties for this flow, which are comparable to those obtained with the Spalart–Allmaras model, the new k-ω model reproduces measurements quite closely, all the way from incompressible speeds to the hypersonic regime.

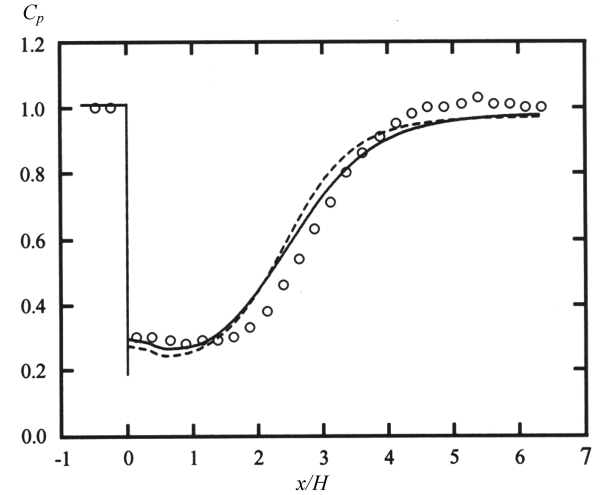

Fig. 15 Effect of the stress limiter on the k-ω model for Mach 2 flow past a backward-facing step: with limiter (solid line), without limiter (dashed line), and Samimy et al. [47] (circles).

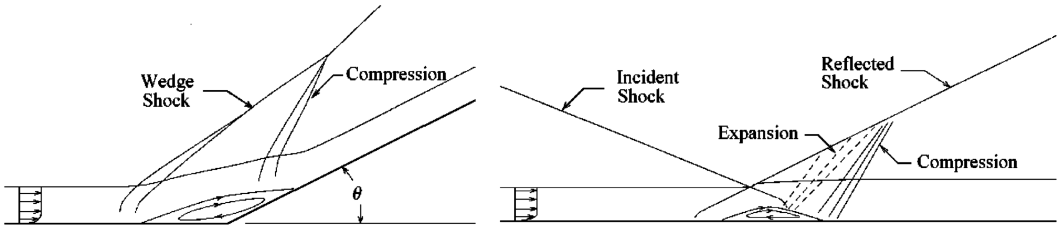

a) Compression-corner flow b) Shock-wave/boundary-layer interaction

Fig. 16 Schematics of supersonic flow into a compression corner and shock-wave/boundary-layer interaction (reflecting shock).

C. Mach 2 Flow Past a Backward-Facing Step

We turn now to compressible flow past a backward-facing step. The case we will discuss has a freestream Mach number of 2.07, the incident boundary layer has a momentum-thickness Reynolds number of $Re_\theta = 1.2 \times 10^4$, and the surface is adiabatic. This flow was investigated experimentally by Samimy et al. [47]. The computation was done with the new k-ω model with and without the stress limiter.

As shown in Fig. 15, with $C_{\text{lim}} = 7/8$, the stress limiter has a barely noticeable effect on the computed surface-pressure coefficient. Computed and measured values of C_p differ by less than 7% for the entire flowfield. Predicted reattachment length with

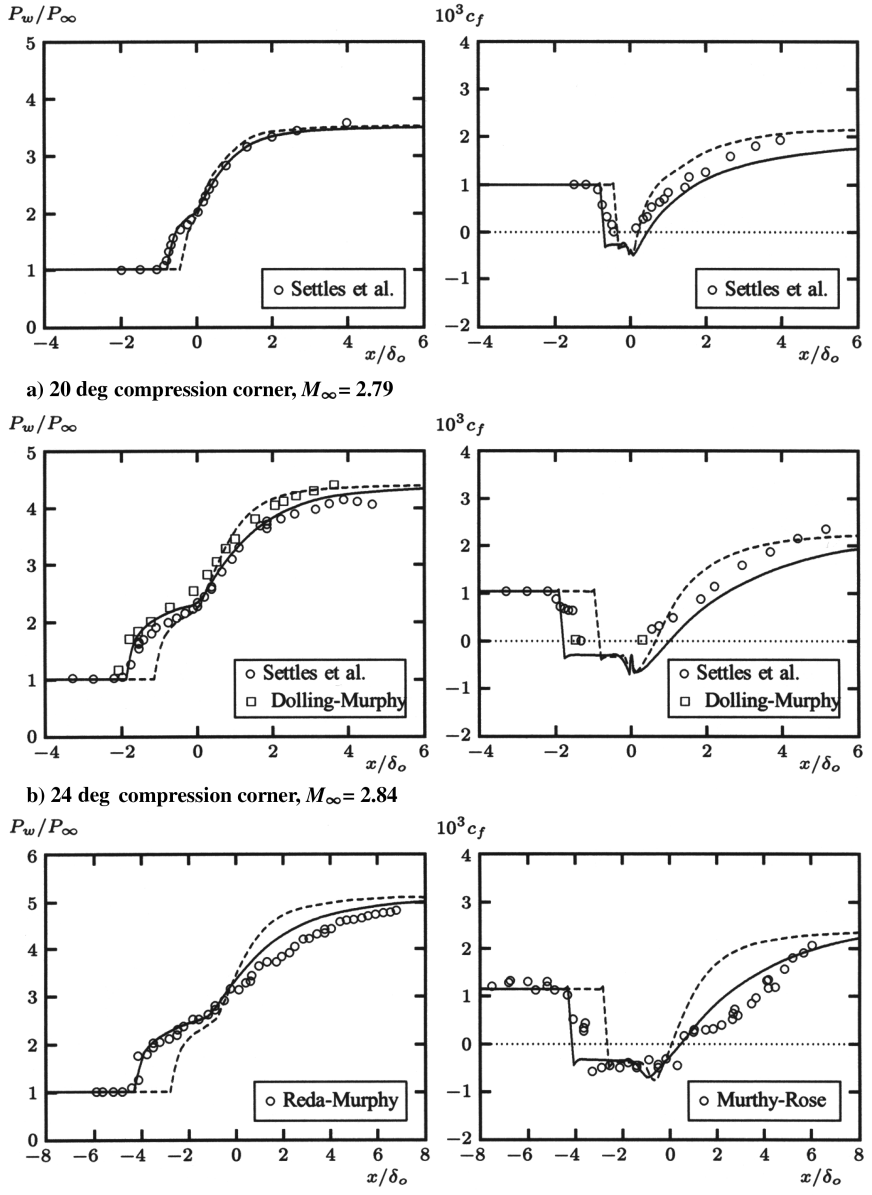

a) 20 deg compression corner, $M_\infty = 2.79$

b) 24 deg compression corner, $M_\infty = 2.84$

c) Shock-wave/boundary-layer interaction, $M_\infty = 2.90$

Fig. 17 Comparison of computed and measured surface pressure and skin friction for Mach 3 shock-separated flows using the new k-ω model: with limiter (solid line), without limiter (dashed line), Settles et al. [50] (circles), Dolling and Murphy [51] (squares), Reda and Murphy [52] (diamonds), and Murthy and Rose [53] (circles).

the limiter is $x_r = 2.67H$. The length decreases to $x_r = 2.55H$ without the limiter. Both values are within a few percent of the value measured by Samimy et al. [47], which is $x_r = 2.76H$. Using $C_{\lim} = 1$ for this flow increases x_r to $2.78H$, which is also quite close to the measured reattachment length. Clearly, the effect is less pronounced than for an incompressible backstep. However, as we will see in the next subsection, with $C_{\lim} = 1$ the stress-limiter effect is far too strong at Mach 3.

D. Mach 3 Compression Corners and Reflecting Shocks

Supersonic flow into a compression corner and reflection of an oblique shock from a flat surface have proven to be the most challenging of all two-dimensional separated-flow applications. Figure 16 sketches these two geometries, including some of the main features of the flow structure for each. Although the geometries are fundamentally different, these flows are nevertheless very similar. Through extensive experimental investigations, Petrov et al. [48] and Chapman et al. [49] developed the *free-interaction concept*. They found that flow details in the vicinity of separation are local and depend almost entirely on Mach number and static-pressure ratio across the separation shock. Thus, if we test a model for compression-corner flows, we should simultaneously test the model for reflecting shocks to check consistency with the free-interaction concept.

Figure 17 compares the computed and measured surface pressure and skin friction for two compression-corner flows and a reflecting-shock case. All three flows have a freestream Mach number close to 3 and have separation bubbles of different sizes. The two compression-corner flows have wedge angles of 20 and 24 deg, corresponding to experiments conducted by Settles et al. [50] and by Dolling and Murphy [51]. Both cases have a wall to adiabatic-wall temperature ratio $T_w/T_{\text{aw}} = 0.88$, corresponding to very mild cooling. The reflecting-shock case was investigated experimentally by Reda and Murphy [52] and by Murthy and Rose [53]. The incident shock makes an angle of 31 deg with the horizontal and turns the flow by 13 deg. The surface for this case is adiabatic.

The graphs include results for the new k-ω model with and without the stress limiter. In all three cases, with the stress limiter, computed and measured surface pressures are very close. Most important, the initial pressure rise in the computed flowfields matches the measured rise. This means that the separation shock is in the same location in the numerical and experimental flowfields. The predicted pressure plateau in the separation bubble and skin friction downstream of reattachment is close to measurements. Discrepancies between computed and measured c_f downstream of reattachment indicates that the rate of recovery from separation and the return to equilibrium conditions is a bit different.

Without the stress limiter, the computed separation-shock location is clearly further downstream than measured, which distorts the entire flowfield.

The similarity between the shapes of the computed p_w/p_∞ and c_f curves for the shock-wave/boundary-layer interaction and the 24 deg compression-corner flow is striking. Because the overall pressure rise is nearly the same for the two flows, this similarity confirms that the k-ω model's predictions are consistent with the free-interaction concept.

The numerical separation points for these flows are further upstream than indicated by oil-flow measurements. Marshall and Dolling [54] indicated that such flows include a low-frequency separation-shock oscillation. Adams [55] found this oscillation in a direct numerical simulation of a Mach 3 compression-corner flow. The time-mean pressure distribution upstream of the corner is affected by these oscillations, for which the frequency content includes substantial energy at time scales of the mean motion. This unsteadiness is responsible for the apparent mismatch between the beginning of the pressure rise and the separation point. Because computations with the k-ω model are so close to measured properties, yet display no low-frequency oscillation of the shock, we can reasonably conclude that the computations effectively incorporate the slow oscillation into the Favre-averaged flow variables.

Figure 18 indicates how the separation-point location for the 24 deg compression-corner flow varies with $C_{\lim}$. As shown, similar to the effect for an incompressible backward-facing step (see Fig. 13), $-x_s$ increases monotonically as $C_{\lim}$ increases. Selecting $C_{\lim} = 7/8$ yields a value of $x_s = -1.82\delta$, which provides a very close match to most details of this flowfield.

Figure 19 shows that using $C_{\lim} = 1$ produces a separation bubble roughly twice the measured size. This explains why Menter's [7] model fares so poorly for this flow [56].

E. Mach 11 Reflecting Shock

We turn now to a hypersonic flow: namely, the Mach 11 shock-wave/boundary-layer interaction investigated by Holden [57]. The incident shock makes a 17.6 deg angle with the surface and increases the static pressure by a factor of 70. The shock angle was adjusted from the precise value used in the experiment to match the overall

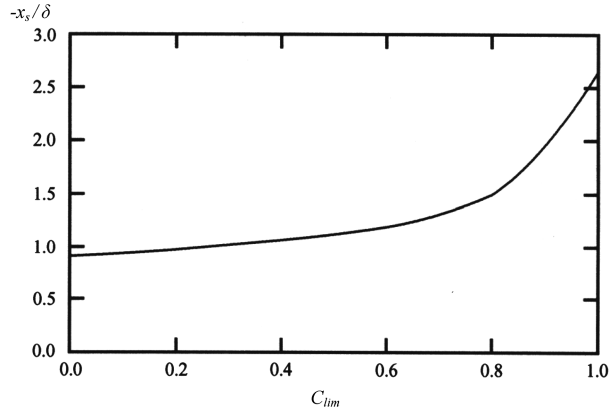

Fig. 18 Effect of the stress-limiter coefficient on computed separation-point location for Mach 3 flow into a 24 deg compression corner.

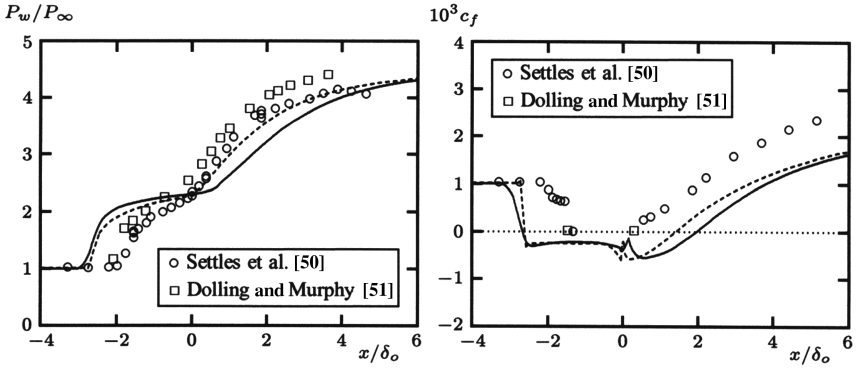

Fig. 19 Comparison of computed and measured surface pressure and skin friction for Mach 3 flow into a 24 deg compression corner: Menter [7] k-ω/k-ε model (solid line), new k-ω model with $C_{\lim} = 1$ (dashed line), Settles et al. [50] (circles), and Dolling and Murphy [51] (squares).

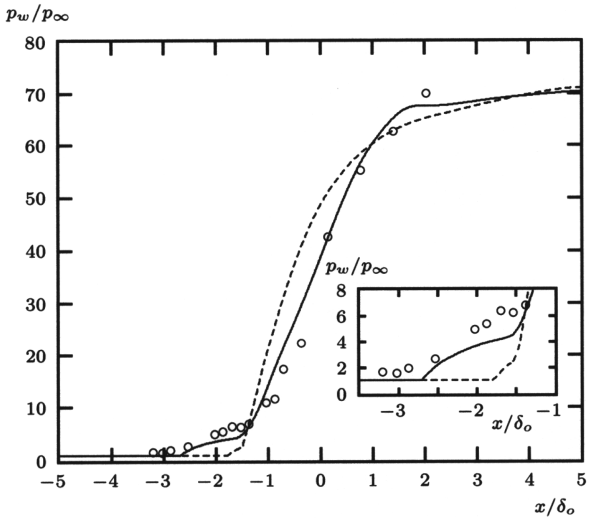

Fig. 20 Effect of the stress limiter on the new k-ω model for a Mach 11 shock-wave/boundary-layer interaction: with limiter (solid line), without limiter (dashed line), and Holden [57] (circles).

inviscid pressure rise for an assumed specific heat ratio $\gamma = 1.4$. The surface is highly cooled with a wall-to-adiabatic-wall temperature ratio of $T_w/T_{aw} = 0.2$.

Figure 20 compares computed and measured surface pressure for the new k-ω model with and without the stress limiter. As shown, the limiter increases separation-bubble length from 0.34 to $1.53\delta_o$. The computed surface-pressure rise is much closer to the measured rise when the limiter is used. As with the Mach 3 applications of the preceding subsection, this indicates that the predicted shock pattern closely matches the experimental pattern. Holden [57] estimated the size of the separation bubble to be about $1.00\delta_o$. The surface-pressure data suggest a separation bubble about twice that size.

As with all of the computations discussed in this paper, the turbulent Prandtl number was chosen to be $Pr_T = 0.89$. In general, for this and other hypersonic shock-separated flows done with the new k-ω model (see Wilcox [14]), computed heat transfer at the reattachment point is about 50% higher than measured. This difficulty is characteristic of turbulence models that base the turbulent heat-flux vector on Reynolds' analogy. As shown by Xiao et al. [58], realistic predictions for hypersonic reattachment point heat transfer can be achieved by constructing additional model equations to compute the heat-flux vector.

V. Conclusions

There are two significant results of the research described in this paper. First, only a small range of values for the cross-diffusion coefficient σ_d exists that yields satisfactory spreading rates for free shear flows (see Figs. 1 and 2). Second, using too large of a value for the stress-limiter strength $C_{\lim}$ causes the k-ω model to predict separated regions much larger than measured for flows above transonic speeds (see Fig. 19).

The new k-ω model retains all of the strengths of previous models developed by the author. Specifically, the model is as accurate for attached boundary layers, backward-facing steps, and mildly separated incompressible flows. The original k-ω model presented by Saffman [2] had five empirical closure coefficients. Of necessity, some of the model's elegance and simplicity was sacrificed to remove sensitivity to freestream boundary conditions and to achieve more realistic predictions for free shear flows. The price was one additional closure coefficient, σ_d, and two empirical closure functions [see Eqs. (11–13)]. And, of course, the model requires a replacement for the linear constitutive relation between Reynolds stresses and mean strain rate used in the original model. The stress limiter is the simplest such relationship available, and it adds just one additional closure function [see Eq. (6)].

Inclusion of a cross-diffusion term in the ω equation 1) greatly improves the model's predictions for all five of the classic free shear flows (see Table 1) and 2) significantly reduces the model's sensitivity to finite freestream boundary conditions on turbulence parameters (see Fig. 4).

With inclusion of a stress limiter, the new k-ω model predicts reasonably close agreement with measured properties of shock-separated flows for transonic, supersonic, and hypersonic regimes. Although discrepancies can be reduced even further by increasing the strength of the limiter in specific cases (most notably for transonic flows), choosing a limiter strength of $C_{\lim} = 7/8$ appears to be the optimum choice for covering the entire range of flow speeds from incompressible to hypersonic.

The fact that all of the results presented in this paper were achieved without any explicit compressibility modifications to the k-ω model is entirely consistent with Morkovin's [59] hypothesis. That is, the effect of density fluctuations on the turbulence is small provided they remain small relative to the mean density. Although the model predicts larger-than-measured values of heat flux at the reattachment point in a hypersonic flow, that is an inaccuracy caused by a faulty constitutive relation rather than a breakdown of Morkovin's hypothesis.

Although not discussed in this paper, the new k-ω model fails to match the measured reduction of spreading rate for a compressible mixing layer. As discussed in great detail by Wilcox [14], density fluctuations for a compressible mixing layer are much larger than in wall-bounded flows and are not small relative to the mean density. Hence, Morkovin's [59] hypothesis fails and the model, like all turbulence models, will require ad hoc compressibility modifications to match measurements.

Appendix A: Numerical Accuracy

The computations presented in this paper were done with several computer programs that apply to three different types of flows: namely, free shear flows, attached boundary layers, and flows with boundary-layer separation. All of these programs, including source code, are included in the textbook by Wilcox [14]. The purpose of this Appendix is to briefly describe the programs and to document the results of an iteration and grid-resolution study for the numerical results discussed in this paper.

In all of the cases, the grid convergence index (GCI) devised by Roache [60] is presented for the most sensitive flow property. This index, based on generalized Richardson extrapolation, provides an excellent measure of the computation's accuracy. The ratio of fine-grid to coarse-grid dimensions is denoted by r. For example, a fine grid with 1.5 times the number of points in the coarse grid would have $r = 1.5$. For a numerical method that is accurate to order p, the GCI for a given flow property ϕ is

$$\text{GCI} = 1.25\frac{|\varepsilon_h|}{r^p - 1}, \qquad \varepsilon_h \equiv \frac{\phi_{\text{fine}} - \phi_{\text{coarse}}}{\phi_{\text{fine}}} \tag{A1}$$

I. Free-Shear-Flow Programs

Three programs named JET, MIXER, and WAKE were used to compute far-field properties of jets, mixing layers, and wakes. All three programs use time-marching methods to solve the nonlinear two-point boundary-value problems attending use of the similarity-solution method for simple turbulent flows. The solution algorithm used is based on implicit Crank–Nicolson [61] differencing. To render straightforward and easy-to-modify programs, each equation

Table A1 Grid-resolution results for spreading rate

Flow	Fine-grid size	r	δ'_{coarse}	δ'_{fine}	GCI
Far wake	201	2	0.32640	0.32600	0.05%
Mixing layer	201	2	0.09599	0.09643	0.19%
Plane jet	201	2	0.10780	0.10740	0.16%
Round jet	201	2	0.09411	0.09388	0.10%
Radial jet	201	2	0.09914	0.09890	0.10%

Table A2 Grid-resolution results for skin friction

Flow	Figure	Fine-grid size	r	$10^3(c_f)_{\text{coarse}}$	$10^3(c_f)_{\text{fine}}$	GCI
Samuel and Joubert experiment [29]	6	201	2	1.30875	1.31154	0.09%
Stratford [30]	6	201	2	0.67697	0.67203	0.31%
Coles Mach 4.5 experiment [31]	7	201	2	1.21393	1.21390	0.00%
Watson Mach 10.3 experiment [31]	7	201	2	0.23706	0.23741	0.06%

Table A3 Grid-resolution results for separated-region size

Flow	Figure	Fine-grid Size	r	Δx_{coarse}	Δx_{fine}	GCI
High Reynolds number incompressible backstep	11	301×163	1.25	7.158	7.070	3.1%
Low Reynolds number incompressible backstep	12	201×163	1.25	7.451	7.280	5.9%
Transonic bump	14	201×101	1.25	0.414	0.410	2.6%
Mach 2 backstep	15	401×201	1.25	2.728	2.672	5.3%
Mach 3 20 deg compression corner	17	401×201	1.41	1.151	1.160	1.1%
Mach 3 24 deg compression corner	17	401×201	1.41	2.785	2.825	2.0%
Mach 3 shock/boundary-layer interaction	17	401×201	1.41	4.603	4.650	1.5%
Mach 11 shock/boundary-layer interaction	19	500×300	1.19	1.519	1.530	2.5%

of a given turbulence model is solved independently using a standard tridiagonal-matrix inversion algorithm.

An additional transformation devised by Rubel and Melnik [62] was used in all three of the free-shear-flow programs that greatly improves numerical accuracy. Because the transformation automatically stretches the transformed distance in regions of rapidly varying flow properties, a grid with equally spaced points can be used. Consequently, as validated by computations on three different finite difference grids, the programs are exactly second-order-accurate (i.e., $p = 2$).

All computations were run until machine accuracy was achieved, which assures that iteration convergence was attained. Table A1 summarizes the results of a grid-resolution study. Computed spreading rate for the five basic free shear flows is listed for finite difference grids with 101 and 201 points. In general, the GCI is even smaller for flow properties throughout the numerical flowfield.

II. Attached Boundary Layers

A program named EDDYBL was used for attached boundary layers. The program applies to attached, compressible, two-dimensional, and axisymmetric boundary layers. It includes the new k-ω model as well as many popular algebraic, one-equation, and two-equation models.

Program EDDYBL uses the Blottner [63] variable-grid method augmented with an algorithm devised by Wilcox [64] to permit large streamwise steps. The program uses adaptive gridding in the streamwise direction, decreasing step size as the number of iterations needed for convergence increases and vice versa. Computations on three different grids show that the effective order of accuracy of the numerical algorithm is $p = 1.9$. Wilcox [14] provided an in-depth discussion of the algorithm.

Table A2 summarizes results of a grid-resolution study. The table includes computed skin friction at the last streamwise station for the four attached boundary-layer cases shown in Figs. 6 and 7. As with the free-shear-flow computations already discussed, the GCI is even smaller for other flow properties throughout the numerical flowfield.

III. Flows with Boundary-Layer Separation

A program named EDDY2C was used for flows with boundary-layer separation. The program uses the MacCormack [41] fully implicit flux-splitting method with Gauss–Seidel line relaxation. Computations on numerous flows with three different grids show that the effective order of accuracy of the numerical algorithm is typically $p = 1.8$.

The flow property that generally takes longest to converge is the size of the separated region. All computations reported in this paper were run long enough to insure iteration convergence, with the maximum residual being reduced by 6 to 10 orders of magnitude. Table A3 includes computed separation-bubble length ($\Delta x = x_r - x_s$) for the shock-separated flows and reattachment length ($\Delta x = x_r$) for the backstep applications. As with the free-shear-flow and boundary-layer computations already discussed, the GCI is even smaller for flow properties throughout the numerical flowfield. For example, the skin-friction and pressure coefficients downstream of reattachment for the backward-facing steps have a GCI of about 1%.

Acknowledgment

The research presented in this paper was totally funded by DCW Industries, Inc.

References

[1] Kolmogorov, A. N., "Equations of Turbulent Motion of an Incompressible Fluid," *Izvestiya Academii Nauk USSR: Physics*, Vol. 6, Nos. 1–2, 1942, pp. 56–58.

[2] Saffman, P. G., "A Model for Inhomogeneous Turbulent Flow," *Proceedings of the Royal Society of London, Series A: Mathematical and Physical Sciences*, Vol. 317, No. 1530, 1970, pp. 417–433. doi:10.1098/rspa.1970.0125

[3] Wilcox, D. C., and Alber, I. E., "A Turbulence Model for High Speed Flows," *Proceedings of the 1972 Heat Transfer and Fluid Mechanics Institute*, Stanford Univ. Press, Stanford, CA, 1972, pp. 231–252.

[4] Wilcox, D. C., "Reassessment of the Scale Determining Equation for Advanced Turbulence Models," *AIAA Journal*, Vol. 26, No. 11, 1988, pp. 1299–1310. doi:10.2514/3.10041

[5] Wilcox, D. C., *Turbulence Modeling for CFD*, 2nd ed., DCW Industries, Inc., La Cañada, CA, 1998.

[6] Speziale, C. G., Abid, R., and Anderson, E. C., "A Critical Evaluation of Two-Equation Models for Near Wall Turbulence," AIAA Paper 90-1481, Seattle, WA, 1990.

[7] Menter, F. R., "Improved Two-Equation k-ω Turbulence Models for Aerodynamic Flows," NASA TM-103975, 1992.

[8] Wilcox, D. C., "A Two-Equation Turbulence Model for Wall-Bounded and Free-Shear Flows," AIAA Paper 93-2905, Orlando, FL, 1993.

[9] Kok, J. C., "Resolving the Dependence on Freestream Values for the k-ω Turbulence Model," *AIAA Journal*, Vol. 38, No. 7, 2000, pp. 1292–1295.

[10] Hellsten, A., "New Advanced k-ω Turbulence Model for High-Lift Aerodynamics," *AIAA Journal*, Vol. 43, No. 9, 2005, pp. 1857–1869. doi:10.2514/1.13754

[11] Coakley, T. J., "Turbulence Modeling Methods for the Compressible Navier-Stokes Equations," AIAA Paper 83-1693, 1983.

[12] Huang, P. G., "Physics and Computations of Flows with Adverse Pressure Gradients," *Modeling Complex Turbulent Flows*, Kluwer, Dordrecht, The Netherlands, 1999, pp. 245–258.

[13] Kandula, M., and Wilcox, D. C., "An Examination of k-ω Turbulence Model for Boundary Layers, Free Shear Layers and Separated Flows," AIAA Paper 95-2317, San Diego, CA, 1995.
[14] Wilcox, D. C., *Turbulence Modeling for CFD*, 3rd ed., DCW Industries, Inc., La Cañada, CA, 2006.
[15] Papp, J. L., and Dash, S. M., "Turbulence Model Unification and Assessment for High-Speed Aeropropulsive Flows," AIAA Paper 2001-0880, 2001.
[16] Schlichting, H., and Gersten, K., *Boundary Layer Theory*, 8th ed., Springer–Verlag, Berlin, 1999.
[17] Andersen, P. S., Kays, W. M., and Moffat, R. J., "The Turbulent Boundary Layer on a Porous Plate: An Experimental Study of the Fluid Mechanics for Adverse Free-Stream Pressure Gradients," Dept. of Mechanical Engineering, Stanford Univ., Rept. HMT-15, Stanford, CA, 1972.
[18] Peng, S.-H., Davidson, L., and Holmberg, S., "A Modified Low-Reynolds Number k-ω Model for Recirculating Flows," *Journal of Fluids Engineering*, Vol. 119, No. 4, 1997, pp. 867–875. doi:10.1115/1.2819510
[19] Launder, B. E., and Sharma, B. I., "Application of the Energy Dissipation Model of Turbulence to the Calculation of Flow Near a Spinning Disc," *Letters in Heat and Mass Transfer*, Vol. 1, No. 2, 1974, pp. 131–138. doi:10.1016/0094-4548(74)90150-7
[20] Lele, S. K., "A Consistency Condition for Reynolds Stress Closures," *Physics of Fluids* Vol. 28, 1985, p. 64. doi:10.1063/1.865126
[21] Pope, S. B., "An Explanation of the Turbulent Round-Jet/Plane-Jet Anomaly," *AIAA Journal*, Vol. 16, No. 3, 1978, pp. 279–281. doi:10.2514/3.7521
[22] Rubel, A., "On the Vortex Stretching Modification of the k-ε Turbulence Model: Radial Jets," *AIAA Journal*, Vol. 23, No. 7, 1985, pp. 1129–1130. doi:10.2514/3.9051
[23] Tanaka, T., and Tanaka, E., "Experimental Study of a Radial Turbulent Jet," *Bulletin of the JSME*, Vol. 19, No. 133, 1976, pp. 792–799.
[24] Witze, P. O., and Dwyer, H. A., "The Turbulent Radial Jet," *Journal of Fluid Mechanics*, Vol. 75, 1976, pp. 401–417. doi:10.1017/S0022112076000293
[25] Yakhot, V., and Orszag, S. A., "Renormalization Group Analysis of Turbulence, 1: Basic Theory," *Journal of Scientific Computing*, Vol. 1, No. 1, 1986, pp. 3–51. doi:10.1007/BF01061452
[26] Fage, A., and Falkner, V. M., "Note on Experiments on the Temperature and Velocity in the Wake of a Heated Cylindrical Obstacle," *Proceedings of the Royal Society of London, Series A: Mathematical and Physical Sciences*, Vol. 135, 1932, pp. 702–705.
[27] Weygandt, J. H., and Mehta, R. D., "Three-Dimensional Structure of Straight and Curved Plane Wakes," *Journal of Fluid Mechanics*, Vol. 282, 1995, p. 279. doi:10.1017/S0022112095000140
[28] Bardina, J., Huang, P. G., and Coakley, T. J., "Turbulence Modeling Validation," AIAA Paper 97-2121, 1997.
[29] Kline, S. J., Cantwell, B. J., and Lilley, G. M. (eds.), *Complex Turbulent Flows*, Stanford Univ., Stanford, CA, 1981.
[30] Stratford, B. S., "An Experimental Flow with Zero Skin Friction Throughout its Region of Pressure Rise," *Journal of Fluid Mechanics*, Vol. 5, 1959, pp. 17–35. doi:10.1017/S0022112059000027
[31] Fernholz, H. H., and Finley, P. J., "A Further Compilation of Compressible Boundary Layer Data with a Survey of Turbulence Data," AGARD AGARDograph 263, Neuilly-sur-Seine, France, 1981.
[32] Klebanoff, P. S., "Characteristics of Turbulence in a Boundary Layer with Zero Pressure Gradient," NACA TN 1247, 1955.
[33] Wieghardt, K., and Tillman, W., "On the Turbulent Friction Layer for Rising Pressure," NACA TM 1314, 1951.
[34] Winter, K., and Gaudet, L., "Turbulent Boundary-Layer Studies at High Reynolds Number at Mach Numbers Between 0.2 and 2.8," Aeronautical Research Council, Research and Memorandum No. 3712, London, 1973.
[35] Durbin, P. A., "On the k-ε Stagnation Point Anomaly," *International Journal of Heat and Fluid Flow*, Vol. 17, No. 1, 1996, pp. 89–90. doi:10.1016/0142-727X(95)00073-Y
[36] Moore, J. G., and Moore, J., "Realizability in Two-Equation Turbulence Models," AIAA Paper 99-3779, 1999.
[37] Bradshaw, P., Ferriss, D. H., and Atwell, N. P., "Calculation of Boundary Layer Development Using the Turbulent Energy Equation," *Journal of Fluid Mechanics*, Vol. 28, Pt. 3, 1967, pp. 593–616. doi:10.1017/S0022112067002319
[38] Saffman, P. G., and Wilcox, D. C., "Turbulence-model Predictions for Turbulent Boundary Layers," *AIAA Journal*, Vol. 12, No. 4, 1974, pp. 541–546. doi:10.2514/3.49282
[39] Wilcox, D. C., and Traci, R. M., "Analytical Study of Freestream Turbulence Effects on Stagnation Point Flow and Heat Transfer," AIAA Paper 74-515, 1974.
[40] Bearman, P. W., "Some Measurements of the Distortion of Turbulence Approaching a Two-Dimensional Bluff Body," *Journal of Fluid Mechanics*, Vol. 53, Part 3, 1972, pp. 451–467. doi:10.1017/S0022112072000254
[41] MacCormack, R. W., "Current Status of Numerical Solutions of the Navier-Stokes Equations," AIAA Paper 85-32, 1985.
[42] Driver, D. M., and Seegmiller, H. L., "Features of a Reattaching Turbulent Shear Layer in Divergent Channel Flow," *AIAA Journal*, Vol. 23, No. 2, 1985, pp. 163–171. doi:10.2514/3.8890
[43] Jovic, S., and Driver, D., "Reynolds Number Effect on the Skin Friction in Separated Flows Behind a Backward-Facing Step," *Experiments in Fluids*, Vol. 18, No. 6, 1995, pp. 464–467. doi:10.1007/BF00208471
[44] Jovic, S., and Driver, D., "Backward-Facing Step Measurements at Low Reynolds Number," NASA TM-108870, 1994.
[45] Bachalo, W. D., and Johnson, D. A., "An Investigation of Transonic Turbulent Boundary Layer Separation Generated on an Axisymmetric Flow Model," AIAA Paper 79-1479, 1979.
[46] Spalart, P. R., and Allmaras, S. R., "A One-Equation Turbulence Model for Aerodynamic Flows," AIAA Paper 92-439, 1992; also *La Recherche Aerospatiale : bulletin Bimestriel de l'Office National d'Etudes et de Recherches Aerospatiales*, No. 1, 1994, p. 5.
[47] Samimy, M., Petrie, H. L., and Addy, A. L., "Reattachment and Redevelopment of Compressible Turbulent Free Shear Layers," *International Symposium on Laser Anemometry*, Vol. 33, American Society of Mechanical Engineers, Fluids Engineering Div., New York, 1985, pp. 159–166.
[48] Petrov, G., Likhusin, V., Nekrasov, I., and Sorkin, L., "Influence of Viscosity on the Supersonic Flow with Shock Waves," *Central Institute of Aviation Motors*, No. 224, 1952 [in Russian].
[49] Chapman, D., Kuehn, D., and Larson, H., "Investigation of Separated Flows in Supersonic and Subsonic Streams with Emphasis on the Effect of Transition," NACA Rept. 1356, 1957.
[50] Settles, G. S., Vas, I. E., and Bogdonoff, S. M., "Details of a Shock Separated Turbulent Boundary Layer at a Compression Corner," *AIAA Journal*, Vol. 14, No. 12, 1976, pp. 1709–1715. doi:10.2514/3.61513
[51] Dolling, D. S., and Murphy, M. T., "Unsteadiness of the Separation Shock-wave Structure in a Supersonic Compression Ramp Flowfield," *AIAA Journal*, Vol. 21, No. 12, 1983, pp. 1628–1634. doi:10.2514/3.60163
[52] Reda, D. C., and Murphy, J. D., "Shock-wave/Turbulent-Boundary-Layer Interactions in Rectangular Channels," *AIAA Journal*, Vol. 11, No. 2, 1973, pp. 139–140. doi:10.2514/3.50445also AIAA Paper 72-715, 1972.
[53] Murthy, V. S., and Rose, W. C., "Wall Shear Stress Measurements in a Shock-Wave/Boundary-Layer Interaction," *AIAA Journal*, Vol. 16, No. 7, 1978, pp. 667–672. doi:10.2514/3.60956
[54] Marshall, T. A., and Dolling, D. S., "Computation of Turbulent, Separated, Unswept Compression Ramp Interactions," *AIAA Journal*, Vol. 30, No. 8, 1992, pp. 2056–2065. doi:10.2514/3.11179
[55] Adams, N., "Direct Simulation of the Turbulent Boundary Layer along a Compression Ramp at $M = 3$ and $Re_\theta = 1685$," *Journal of Fluid Mechanics*, Vol. 420, 2000, pp. 47–83. doi:10.1017/S0022112000001257
[56] Forsythe, J. R., Strang, W. Z., and Hoffmann, K. A., "Validation of Several Reynolds-Averaged Turbulence Models in a 3-D Unstructured Grid Code," AIAA Paper 00-2552, 2000.
[57] Holden, M. S., "A Study of Flow Separation in Regions of Shock Wave-Boundary Layer Interaction in Hypersonic Flow," AIAA Paper 78-1168, 1978.
[58] Xiao, X., Edwards, J. R., Hassan, H. A., and Gaffney, R. L., Jr., "Role of Turbulent Prandtl Number on Heat Flux at Hypersonic Mach Numbers," AIAA Paper 2005-1098, 2005.
[59] Morkovin, M. V., "Effects of Compressibility on Turbulent Flow," *The Mechanics of Turbulence*, edited by A. Favre, Gordon and Breach, New York, 1962, p. 367.
[60] Roache, P. J., *Verification and Validation in Computational Science and Engineering*, Hermosa, Albuquerque, NM, 1998.

[61] Crank, J., and Nicolson, P., "A Practical Method for Numerical Evaluation of Solutions of Partial Differential Equations of the Heat-Conduction Type," *Proceedings of the Cambridge Philosophical Society (Mathematical and Physical Sciences)*, Vol. 43, No. 50, 1947, pp. 50–67.

[62] Rubel, A., and Melnik, R. E., "Jet, Wake and Wall Jet Solutions Using a k-ε Turbulence Model," AIAA Paper 84-1523, 1984.

[63] Blottner, F. G., "Variable Grid Scheme Applied to Turbulent Boundary Layers," *Computer Methods in Applied Mechanics and Engineering*, Vol. 4, No. 2, 1974, pp. 179–194. doi:10.1016/0045-7825(74)90033-4

[64] Wilcox, D. C., "Algorithm for Rapid Integration of Turbulence Model Equations on Parabolic Regions," *AIAA Journal*, Vol. 19, No. 2, 1981, pp. 248–251. doi:10.2514/3.7766

P. Givi
Associate Editor